

A Constraint on the Amount of Hydrogen from the CO Chemistry in Debris Disks

KAZUNARI IWASAKI ¹, HIROSHI KOBAYASHI ², AYA E. HIGUCHI ³, AND YURI AIKAWA⁴

- ¹ *Center for Computational Astrophysics, National Astronomical Observatory of Japan, Osawa, Mitaka, Tokyo 181-8588, Japan, kazunari.iwasaki@nao.ac.jp*
² *Department of Physics, Nagoya University, Furo-cho, Chikusa-ku, Nagoya, Aichi 464-8602, Japan*
³ *Division of Science, School of Science and Engineering, Tokyo Denki University, Ishizaka, Hatoyama-machi, Hiki-gun, Saitama 350-0394, Japan*
⁴ *Department of Astronomy, Graduate School of Science, The University of Tokyo, 7-3-1 Hongo, Bunkyo-ku, Tokyo 113-0033, Japan*

ABSTRACT

The faint CO gases in debris disks are easily dissolved into C by UV irradiation, while CO can be reformed via reactions with hydrogen. The abundance ratio of C/CO could thus be a probe of the amount of hydrogen in the debris disks. We conduct radiative transfer calculations with chemical reactions for debris disks. For a typical dust-to-gas mass ratio of debris disks, CO formation proceeds without the involvement of H₂ because a small amount of dust grains makes H₂ formation inefficient. We find that the CO to C number density ratio depends on a combination of $n_{\text{H}} Z^{0.4} \chi^{-1.1}$, where n_{H} is the hydrogen nucleus number density, Z is the metallicity, and χ is the FUV flux normalized by the Habing flux. Using an analytic formula for the CO number density, we give constraints on the amount of hydrogen and metallicity for debris disks. CO formation is accelerated by excited H₂ either when the dust-to-gas mass ratio is increased or the energy barrier of chemisorption of hydrogen on the dust surface is decreased. This acceleration of CO formation occurs only when the shielding effects of CO are insignificant. In shielded regions, the CO fractions are almost independent of the parameters of dust grains.

1. INTRODUCTION

Planets are believed to be formed in protoplanetary disks (PPDs) containing gas and dust. The dissipation timescale of PPDs, especially that of gaseous component, is of special importance for planetary system formation. The gas giant planets need to be formed prior to the significant dispersal of gas in disks (Mizuno et al. 1978; Tanigawa & Ikoma 2007) and the gas dispersal may then lead to long term orbital instabilities of protoplanets that trigger their impacts (Iwasaki et al. 2001). The giant impacts between protoplanets are believed to form the terrestrial planets in the solar system.

Infrared emission from PPDs decreases in several million years (Haisch et al. 2001). Older faint disks around main-sequence stars are called debris disks (Hughes et al. 2018, for review), which might be explained by dust production due to collisional cascades starting from disruptive collisions of kilometer or larger bodies. That may be induced by planet formation events after gas dispersal such as giant impacts for terrestrial planet formation (e.g., Genda et al. 2015) or planetary accretion in outer disks (Kobayashi & Löhne 2014). Sub-mm observations showed some debris disks with ages of several 10 Myrs still have molecular CO gas (Hughes et al. 2008;

Dent et al. 2014; Moór et al. 2019). In the present work we aim to investigate if the gas in debris disks is a primary origin, i.e., the gas of PPDs is not fully dispersed, or secondary origin. This question is directly linked to how and when the disk gas dissipates.

In the secondary scenario, the observed CO is produced from solid bodies via collisions (Kral et al. 2016, 2017; Matrà et al. 2015, 2017, 2018). However, CO is photo-dissociated rapidly. For β Pictoris whose disk has CO with $\sim 3 \times 10^{-5} M_{\oplus}$, the dissociation timescale is about ~ 100 years so that the mass production of CO during the stellar age is estimated to be $\sim 3 M_{\oplus}$, where M_{\oplus} is the Earth mass (cf. Kral et al. 2016). The IR observations for comets by AKARI infer the fraction of CO to H₂O ~ 0.1 (Ootsubo et al. 2012). Total solid bodies required for the observed gas is simply estimated from the CO mass and fraction to be $30 M_{\oplus}$, which is comparable to or larger than that of the solar system.

The gas production due to sublimation strongly depends on the temperature of parent bodies. Using the condensation temperature, the sublimation timescale is estimated to be 0.003 yrs for kilometer-sized CO bodies with 50 K, while it may be somehow longer for mixed ices. However, the timescale is much shorter than the

ages of debris disks. It would thus be difficult to keep $\sim 3M_{\oplus}$ of CO in the icy bodies, unless there was a steady inflow from the outer colder regions. Carbon dioxide, CO_2 , can be another reservoir. CO observed around comets in our solar system is mainly explained by the photo-dissociation of CO_2 (Weaver et al. 2011) so that CO might be less abundant than CO_2 in comets. Outgassing CO_2 changes into CO via photo-dissociation. Collisional vaporization occurs due to shock heating (Ahrens & O’Keefe 1972; Kurosawa et al. 2010), so that high speed impacts ($\lesssim 5$ km/s) are required even for vaporization of volatile materials (e.g., Okeefe & Ahrens 1982; Kraus et al. 2011). The collisional velocities are estimated to be $1 \text{ km s}^{-1}(e/0.1)(M_*/M_{\odot})^{1/2}(r/10 \text{ au})^{1/2}$, where e and r are the orbital eccentricities and semi-major axes of colliding bodies, respectively, M_* is the mass of the central star, and M_{\odot} is the solar mass (e.g., Kobayashi & Löhne 2014). The collisional velocities of bodies with $e \sim 0.1$ beyond 10 au are much slower than the vaporization velocity. The collisional outgassing of CO_2 from cometary bodies is therefore difficult beyond 10 au, where CO gas is observed in debris disks. In summary, in the secondary-origin scenario, a large amount of reservoir ice is required, while it should be sublimated efficiently beyond > 10 au.

If the gas in debris disks is a primary origin, or is a mixture of primary and secondary components, CO can be reformed from C^+ and C atoms in the gas phase. The required CO reservoir is then significantly reduced compared with the case of purely secondary gas. Higuchi et al. (2017) showed that the abundance ratio of atomic carbon to CO can be a probe of the abundance of H_2 relative to carbon, i.e. the metallicity of gas in debris disks. If the gas is a remnant of PPDs, the metallicity is expected to be close to that of the interstellar medium (ISM). On the other hand, if gas is supplied from solid bodies, the metallicity is much larger than the ISM value while hydrogen is provided by H_2O desorbed from solid bodies.

Although the CO chemistry in debris disks was investigated by many authors (Kamp & Bertoldi 2000; Kamp et al. 2003; Gorti & Hollenbach 2004; Hughes et al. 2008; Roberge et al. 2013), the elemental abundances in their models are not different from those in the ISM significantly. The metallicity can be different from the ISM value, depending on the origin of gas. Thus, in this paper, we examine how the CO chemistry depends on metallicity by calculating detailed chemical reactions and thermal processes, and the radiative transfer including exact line transfers in the debris disks.

This paper is organized as follows: one-dimensional plane-parallel PDR calculations. The results of the PDR

calculations are described and an analytical formula for the amount of CO is developed on the basis of the plane-parallel PDR calculations in Section 3. Astrophysical implications are discussed in Section 4. Finally, our results are summarized in Section 5.

2. METHODS AND MODELS

2.1. Numerical Methods

The Meudon PDR code version 1.5.4 (<http://pdr.obspm.fr/>) is a publicly available photon dominated region (PDR) code which is designed to model a stationary plane-parallel slab of gas and dust controlled by far-ultraviolet (FUV) photons (Le Petit et al. 2006). A plane-parallel slab is illuminated by a radiation field penetrating from the left-side of the slab.

The Meudon code solves the radiative transfer at each point in the slab, taking into account dust extinction and line absorption of gaseous species. We use the exact method described in Goicoechea & Le Bourlot (2007) which allows us to take into account overlapping of the H , H_2 , and CO UV absorption lines. For the H_2 line transfer, we define a value of $J_{\text{max}} = 3$ under which the exact method is used. The FGK approximation proposed by Federman et al. (1979) is used for all electric transitions for $J_l \geq J_{\text{max}}$, where J_l is the lower level of Lyman and Werner transitions. We do not take into account the exact line transfer for ^{13}CO and C^{18}O .

Coupled with the radiative transfer, the full level population system of a number of species, including H_2 and CO, is computed from the detailed balance between radiative transitions, collisional transitions, transitions due to the cosmic microwave background, formation and destruction processes both in the gas phase and on dust grains (Le Petit et al. 2006).

This treatment allows us to evaluate the H_2 self-shielding effect more accurately than using the fitting formula provided by Draine & Bertoldi (1996), which has been used in most studies. Furthermore, the accurate calculation of the level populations provides the accurate rates of chemical reactions associated with excited H_2 , which will be discussed in Section 3.3. Similarly, the shielding effect of CO is calculated more accurately than using the table from Visser et al. (2009).

The Meudon code calculates the thermal equilibrium of gas and dust grains. For gas temperature, heating processes (including the photo-electric heating on dust, exothermic chemical reactions, and cosmic rays) are balanced with cooling processes (including infrared and millimeter emission from ions, atoms, and molecules). The treatment of dust grains is explained in Section 2.4. Chemical and thermal equilibria determine the abundances of each chemical species at each position.

In order to investigate the basic properties of the chemical structure of debris disks, in Section 3, we conduct simple plane-parallel PDR calculations of a semi-infinite gas slab with a uniform density illuminated by stellar radiation fields and the interstellar radiation field (ISRF).

We should note that the Meudon PDR code is not applicable directly to the multi-dimensional disk geometry because it is designed for the one-dimensional plane-parallel geometry. In debris disks, we should take into account the geometrical dilution of the stellar radiation and vertical ISRF. Nevertheless, we will find that the main underlying physics of debris disks can be approximated by the findings from the one-dimensional plane-parallel PDR calculations. In Section 4.2, we compare the observational results with the predictions obtained by applying the findings of the plane-parallel models to disk models.

2.2. Modifications to the Meudon Code

We made some modifications to the Meudon code because it is not designed for debris disks.

Firstly, we modified the calculation of the photo-dissociation of CO^+ . In calculating the photo-dissociation rate of species, the Meudon code divides the species into two groups. For one group, the photo-dissociation rate is estimated from a fitting formula, which is a form of $\propto \exp(-\beta A_V)$, assuming the radiation field to be the ISRF (van Dishoeck et al. 2006), where β is the fitting parameter. The rate is scaled by the ratio of the total UV flux to the ISRF flux. While this formulation is efficient and is often used in PDR calculations of debris disks, it can be inaccurate when the SED of the radiation field is different from the ISRF. In addition, the possible shielding of photo-cross sections that resonate with absorption lines is not considered in the exponential form. Since dust grains in debris disks are larger than those found in the ISM, β is expected to be inaccurate.

For the other group, the photo-dissociation rate is computed directly from $\int \sigma_\lambda I_\lambda / h\nu d\lambda$; σ_λ is the photo-dissociation cross section and I_λ is the radiation intensity summed over all incidence angles. This treatment allows us to evaluate the photo-dissociation consistent with the local radiation field at each position. It is however computationally expensive and used only for important species.

In the Meudon PDR code, CO^+ was included in the former group where the fitting formula is used although CO^+ is one of the most important species to form CO in debris disks. In this work, the photo-dissociation rate of CO^+ is calculated from the numerical integration of

$\int \sigma_\lambda I_\lambda / h\nu d\lambda$, where σ_λ is taken from Lavendy et al. (1993) (also see Heays et al. 2017), and tabulated as a function of the wavelength.

One of the important molecules to form CO in our results is the hydroxyl radical OH, whose photo-dissociation rate is computed directly from the integration of photo-reaction cross sections. It is dissociated by photons with wavelengths longer than 1100 Å. In the adopted radiation fields, the photo-dissociation rate of OH is mainly determined by the $1^2\Sigma^-$ channel, which absorbs photons with ~ 1600 Å (van Dishoeck & Dalgarno 1983). We will define a normalized UV flux dissociating OH in Section 2.3.

Secondly, we modified the rate coefficient of an endothermic reaction of $\text{O} + \text{H}_2 \rightarrow \text{OH} + \text{H}$, which is one of the most important reactions to form CO. The Meudon PDR code treats endothermic reactions of C^+ , S^+ , O, and OH with H_2 , taking into account excited states of H_2 . Except for reactions of $\text{C}^+ + \text{H}_2$ and $\text{S}^+ + \text{H}_2$ ¹ the rate coefficients were calculated assuming that all the internal energies are used to overcome an activation barrier or an endothermicity. In order to calculate the reaction rate of $\text{O} + \text{H}_2 \rightarrow \text{OH} + \text{H}$ more accurately, we use the fitting formulae for the rate coefficient of $\text{O} + \text{H}_2(v) \rightarrow \text{OH} + \text{H}$ for $v = 0, 1, 2$, and 3 derived by Agúndez et al. (2010) based on the theoretical calculations by Sultanov & Balakrishnan (2005). The reaction rates for $v > 3$ are replaced by that for $v = 3$, where v is the vibrational quantum number. As a result, the total reaction rate may be underestimated. Recently, precise rates especially for $v > 3$ have been estimated by Veselinova et al. (2021)².

Thirdly, we do not consider heating owing to the dielectronic recombination. In the Meudon code, for simplicity, the electron captured in an upper electronic level is assumed to be de-excited only through collisions, resulting in gas heating. The density range considered in this paper is so low that most of transitions in the cascade of the captured electron will occur through spontaneous emissions. We only consider gas cooling owing to the removal of the kinetic energy of recombined electron.

2.3. Incident Radiation Fields

We consider two kinds of radiation fields which are incident on the edge of a semi-infinite gas slab.

¹ To estimate the enthalpic chemical reaction rates, the Meudon PDR code uses the results of the theoretical studies done by Zanchet et al. (2013b) and Herráez-Aguilar et al. (2014) for $\text{C}^+ + \text{H}_2 \rightarrow \text{CH}^+ + \text{H}$ and by Zanchet et al. (2013a) for $\text{S}^+ + \text{H}_2 \rightarrow \text{SH}^+ + \text{H}$.

² O and H_2^* with $v > 3$ does not affect the CO formation because the H_2^* ($v > 3$) fractions are too small to affect the CO formation.

One is the ISRF (Habing 1968; Draine 1978; Mathis et al. 1983). The ISRF is given by the summation of four components. One is the ISRF from far- to near-ultraviolet; an expression of the first component is given by

$$I_{\text{ISRF}}(\lambda) = 107.192 \left(\frac{\lambda}{1 \text{ \AA}} \right)^{-2.89} \times \left[\tanh \left(4.07 \times 10^{-3} \left(\frac{\lambda}{1 \text{ \AA}} \right) - 4.5991 \right) + 1 \right] \text{ erg cm}^{-2} \text{ s}^{-1} \text{ \AA}^{-1} \text{ sr}^{-1} \quad (1)$$

for $\lambda \geq 912 \text{ \AA}$ (Mathis et al. 1983)³. The second ISRF component is supplied by cold stars and is expressed as a combination of three black bodies at 6184, 6123, and 2539 K. The third component comes from the dust thermal emission which is estimated by the DustEM code (Compiègne et al. 2011). The forth ISRF component is the cosmic microwave background radiation given by a black body at 2.73 K.

The other radiation field is the stellar emission taken from ATLAS9 (Kurucz 1992; Howarth 2011). We consider two spectral types of A5V and A1V. The effective temperatures T_{eff} of the A5V and A1V stars are 8250 K and 9000 K, respectively. The metallicities of the stars are set to the solar value. The surface gravity is fixed to $\log_{10} g = 4$. Examples of the A5V and A1V stars are β Pictoris (Lecavelier des Etangs et al. 2001) and 49 Ceti (Roberge et al. 2013), respectively.

As the stellar radiation incident into the slab, the radiation field at a representative distance of 50 au from the star is adopted. The mean intensities at 50 au are shown in Figure 1.

We parameterize the UV fluxes that dissociate species which are important to form CO. The following two ranges of wavelengths are focused on.

One wavelength range is $912 \text{ \AA} < \lambda < 1100 \text{ \AA}$, which is shown by the gray region in Figure 1. The photons in this wavelength range photo-dissociate CO and H₂, and photo-ionize C⁰. The FUV photon number flux integrated over the wavelength range is denoted by $F_{\text{FUV,CO}}$, and is often measured in units of the Habing (1968) field flux, $F_{\text{H}} \equiv 1.2 \times 10^7 \text{ cm}^{-2} \text{ s}^{-1}$ (Bertoldi & Draine 1996). The normalized incident FUV photon number flux $\chi_{\text{co}} \equiv F_{\text{FUV,CO}}/F_{\text{H}}$ ⁴ is given by

$$\chi_{\text{co}} = \chi_{\text{co,star}} + \chi_{\text{co,ISRF}}/2, \quad (2)$$

³ Equation (1) is a fitting function of the results of (Mathis et al. 1983) as shown in the manual of the Meudon PDR code.

⁴ In this paper, $\chi_{\text{co}} = 1$ refers to an FUV field whose energy density at the surface of the gas slab is equal to that of the Habing field considering all 4π steradian in the free-space.

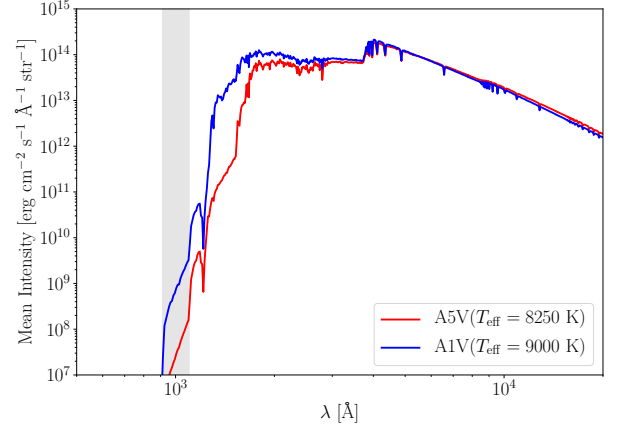


Figure 1. Mean intensities of the stellar radiation of A5V (red) and A1V (blue) stars at a representative distance of 50 au from the central star as a function of wavelength. The FUV photons within the gray region induces photo-dissociation of H₂ and CO, and photo-ionization of C⁰.

where $\chi_{\text{co,star}}$ indicates the normalized stellar FUV flux at a distance of 50 au from the central star, and $\chi_{\text{co,ISRF}} = 1.3$ is the normalized ISRF flux derived from Equation (1).

The other wavelength range is considered to characterize the OH photo-dissociation rate. The cross section of photo-dissociation of OH adopted in the Meudon PDR code has the two broad peaks centered around $\lambda \sim 1090 \text{ \AA}$ ($3 \text{ }^2\Pi$) and $\lambda \sim 1600 \text{ \AA}$ ($1 \text{ }^2\Sigma^-$) (van Dishoeck & Dalgarno 1983, 1984; Heays et al. 2017). The latter peak mainly contributes to the OH photo-dissociation while the contribution from the former peak is negligible. This is because as shown in Figure 1 the intensities of the stellar radiation increase rapidly with wavelength in the corresponding wavelength range. Considering that the intensities of the stellar radiation are an increasing function of wavelength within the latter peak, we set a wavelength range of $1600 \text{ \AA} \leq \lambda \leq 1700 \text{ \AA}$, which corresponds to the long wavelength half of the latter peak. The OH photo-dissociation rate is roughly proportional to the FUV photon number flux integrated over this wavelength range, which is denoted by $F_{\text{FUV,OH}}$. For convenience, we use the normalized FUV flux $\chi_{\text{oh}} \equiv F_{\text{FUV,OH}}/10^{12} \text{ cm}^{-2} \text{ s}^{-1}$.

From the stellar spectra of the A5V and A1V stars shown in Figure 1, one derives that χ_{co} are 1.4 and 31, respectively. The contribution of the ISRF to χ_{oh} is negligible, and $\chi_{\text{oh}} = 2.4$ for A5V and 24 for A1V, respectively.

In this paper, the models with ($\chi_{\text{co}} = 1.4$, $\chi_{\text{oh}} = 2.4$) and those with ($\chi_{\text{co}} = 31$ and $\chi_{\text{oh}} = 24$) are referred to "weak-FUV" and "strong-FUV", respectively.

2.4. Dust Properties

Dust grains play important roles in at least three processes. First, they are responsible for absorption and scattering of photons. Second, they work as a catalyst in some chemical reactions. For instance, H_2 forms on the surface of dust grains rather than by gas phase reactions. Third, they contribute to thermal processes through photo-electric heating and collision with the gas. These processes depend significantly on the dust properties: the size distribution, dust-to-gas mass ratio, and chemical compositions.

2.4.1. Size Distribution

One of the differences of the debris disk from the ISM is absence of small dust grains. The small dust grains with radii smaller than $\sim 1 \mu\text{m}$ are blown out by the radiation pressure of stellar photons (Burns et al. 1979; Kobayashi et al. 2008, 2009). Absence of the small dust grains reduces the visual extinction, the H_2 formation rate, and the photo-electric heating rate for a given dust-to-gas mass ratio. For simplicity, we consider spherical dust grains whose radii are denoted by a . The power-law grain size distribution $n(a) \propto a^{-3.5}$ is assumed, where $n(a)da$ is the number density of the dust grains with the radius range from a to $a + da$ (Mathis et al. 1977). This power-law size distribution is controlled by the collisional cascade (Dohnanyi 1969; Tanaka et al. 1996), although the power-law index could be modulated due to the size dependence of collisional strength (Kobayashi & Tanaka 2010). In this work, the minimum and maximum radii of the dust grains are fixed to $a_{\min} = 1 \mu\text{m}$ and $a_{\max} = 10 \mu\text{m}$. We will discuss that our results do not depend directly on the size distribution in Section 3.1.

2.4.2. Composition

The dust grains are assumed to be a mixture of graphite and silicon. The absorption and scattering coefficients of dust grains are calculated by averaging those of the graphite and silicon in a ratio of 7 : 3, taking into account the size distribution. The heat capacity of the dust grains, which is used to determine the dust temperature at each dust size and position, is computed assuming the mixed composition. The absorption/scattering coefficients and heat capacity at each dust size are computed by Laor & Draine (1993) and Draine & Li (2001).

2.4.3. Charge of Dust Grains

In addition to the FUV flux, the charge of dust grains characterizes the photo-electric yield on the dust grain. The Meudon code takes into account the probability distribution function of the dust charge for each dust size

$f(a, Q)$, which is determined by collisional charging and photo-electric ionization (Bakes & Tielens 1994), where Q is the dust charge.

As the grain size increases, the photo-electric ionization rate increases faster than the recombination rate. As a result, the charge of dust grains increases with a . Since the maximum grain size considered in this work is up to 1 cm, a great number of the charge grid is required.

To reduce the computational cost, we approximate the charge distribution function at each grain size $f(a, Q)$ by a delta function of $\delta(Q - \langle Q \rangle_a)$, where Q is the dust charge and $\langle Q \rangle_a$ is the mean charge for the grain size a . The validity of the approximation $f(a, Q) = \delta(Q - \langle Q \rangle_a)$ is confirmed.

2.4.4. Dust-to-gas Mass Ratio

Since the dust-to-gas mass ratio f_{dg} of debris disks is unknown observationally and theoretically, a wide range of f_{dg} is considered in the present work. Using the size distribution $n(a)$, the dust-to-gas mass ratio is expressed as

$$f_{\text{dg}} \equiv \frac{1}{\mu_{\text{C}} m_{\text{C}} n_{\text{C}}} \frac{4\pi}{3} \rho_{\text{gr}} \langle a^3 \rangle n_{\text{d}}, \quad (3)$$

where

$$\langle g(a) \rangle \equiv \frac{1}{n_{\text{d}}} \int_{a_{\min}}^{a_{\max}} g(a) n(a) da, \quad (4)$$

$n_{\text{d}} = \int_{a_{\min}}^{a_{\max}} n(a) da$ is the total number density of dust grains, m_{x} and n_{x} are the mass and number density of element “x”, respectively, μ_{x} is the mean molecular weight per element “x” nucleus, and $\rho_{\text{gr}} = 2.62 \text{ g cm}^{-3}$ is the internal density of the dust grains. We should note that the gas mass density is expressed as $\mu_{\text{C}} m_{\text{C}} n_{\text{C}}$ because the gas component is considered on the basis of carbon. The gas metallicity is denoted by Z , and the elemental abundances of the gas phase used in the present work are shown in Table 1 for the solar metallicity $Z = 1$. When Z changes, the relative abundances among metals are fixed. From Table 1, μ_{C} is given by

$$\mu_{\text{C}}(Z) = 883 (Z^{-1} + 6.6 \times 10^{-3}). \quad (5)$$

In the context of PPDs, n_{d} is often determined from Equation (3) at a given f_{dg} . By contrast, we use the fact that in debris disks, the amount of dust grains is constrained by the optical depth at V band, which is often estimated from the fraction of the disk luminosity to stellar luminosity. The most practical criterion for debris disks is $\tau < 8 \times 10^{-3}$ (Hughes et al. 2018), where τ denotes a typical vertical optical depth of debris disks. A typical optical depth along the mid-plane τ_{mid} is given by $\tau \theta^{-1}$, where θ is the aspect ratio of debris disks.

atom	relative abundance of the gas phase	reference
He	0.1	
C	1.32×10^{-4}	1
N	7.5×10^{-5}	2
O	3.2×10^{-4}	3
Ne	6.9×10^{-5}	4
Si	8.2×10^{-7}	5
S	1.0×10^{-8}	6
Ar	3.29×10^{-6}	7
Fe	1.5×10^{-8}	1

Table 1. Relative elemental abundances of the gas phase with respect to hydrogen for $Z = 1$. (1) [Savage & Sembach \(1996\)](#), (2) [Meyer et al. \(1997\)](#), (3) [Meyer et al. \(1998\)](#), (4) [Ádámkóvics et al. \(2011\)](#), (5) [Morton \(1975\)](#), (6) [Tieftrunk et al. \(1994\)](#), (7) [Lodders \(2008\)](#).

The mean free path ℓ of a photon for dust absorption depends on the grain size distribution as follows:

$$\ell = (n_d \langle Q_{\text{abs}} \pi a^2 \rangle)^{-1}. \quad (6)$$

In the integration, the absorption coefficient Q_{abs} can be set to be unity because $2\pi a/\lambda > 1$ is satisfied for $a \geq 1 \mu\text{m}$ at the V band. Eliminating n_d using Equations (3) and (6), one obtains

$$f_{\text{dg}} = 1.74 \times 10^{23} \text{ cm}^{-3} \frac{\langle a^3 \rangle}{\langle a^2 \rangle} \mu_{\text{C}}^{-1} \mathcal{N}_{\text{C}, \tau_{\text{mid}}=1}^{-1}, \quad (7)$$

where $\mathcal{N}_{\text{C}, \tau_{\text{mid}}=1} = n_{\text{C}} \ell$ is the mid-plane carbon nucleus column density of the gas phase at $\tau_{\text{mid}} = 1$ of the dust opacity at V band. The values of f_{dg} adopted in our PDR calculations will be shown in Section 2.5.

As mentioned in Section 2.4.1, the size distribution $n(a) \propto a^{-3.5}$ is used, and $\langle a^3 \rangle / \langle a^2 \rangle = \sqrt{a_{\text{min}} a_{\text{max}}}$.

2.4.5. Temperature of Dust Grains

In the Meudon PDR code, the temperature of dust grains T_{gr} is computed from the energy balance between absorption of the radiation and thermal emission at each grain radius bin. For reference, we here show the grain temperature given by [Hughes et al. \(2008\)](#) as follows:

$$T_{\text{gr}} = 10^2 \text{ K} \left(\frac{L_*}{10 L_{\odot}} \right)^{0.2} \left(\frac{a}{1 \mu\text{m}} \right)^{-0.2} \left(\frac{r}{50 \text{ au}} \right)^{-0.4}, \quad (8)$$

where L_* is the stellar luminosity, a is the grain radius, and r is the distance from the central star. The dust temperatures obtained the PDR calculations are consistent with Equation (8).

2.4.6. Grain Surface Chemistry

The Meudon code takes into account H_2 and HD formation with the Langmuir-Hinshelwood (LH) and the Eley-Rideal (ER) mechanisms ([Le Bourlot et al. 2012](#)). The grain-surface chemistry for other species heavier than H_2 and HD is not included in this study because photo-desorption is so efficient that heavy species are difficult to freeze out on the grain surface (e.g., [Grigorieva et al. 2007](#)).

In debris disks, the most important H_2 formation mechanism on dust grains is the ER mechanism involved by chemisorption of H atoms. This is because the dust temperatures, which are as high as ~ 100 K as shown in Equation (8), are so high that a hydrogen atom physisorbed on the grain surface evaporates before it combines with another hydrogen atom.

In the ER mechanism, there are several free parameters in the Meudon PDR code. One is a sticking coefficient $\alpha(T)$, which approaches zero for high temperatures because the hydrogen atom cannot stick on the dust grains owing to the excess kinetic energy. The Meudon PDR code adopts the empirical form $\alpha(T) = 1/(1 + (T/T_{\text{stick}})^{\beta})$, where $T_{\text{stick}} = 464$ K and $\beta = 3/2$ are adopted ([Le Bourlot et al. 2012](#)).

Another parameter is T_{chem} corresponding to the energy barrier that a hydrogen atom overcomes to reach a chemisorption site on the grain surface. The H_2 formation rate is highly sensitive to T_{chem} because the probability of overcoming the energy barrier is proportional to $\exp(-T_{\text{chem}}/T)$. Nonetheless, T_{chem} is highly uncertain. Its value depends on the surface condition and composition of dust grains. The energy barrier of chemisorption onto a perfect graphite surface is as high as ~ 2000 K (e.g., [Sha et al. 2002](#), by using quantum mechanics). This has been confirmed by the experimental study of a highly ordered pyrolytic graphite in the laboratory done by [Zecho et al. \(2002\)](#). By contrast, topological defects on the carbonaceous surface decrease T_{chem} , and can make chemisorption almost barrierless ($T_{\text{chem}} \sim 10 - 100$ K), depending on structures ([Ivanovskaya et al. 2010](#)). Experiments of chemisorption of H on porous, defective, aliphatic carbon surfaces have found that the activation energy is as low as ~ 70 K ([Mennella 2006](#)). By contrast, in the cases with silicate, quantum chemical calculations revealed $T_{\text{chem}} \sim 300$ K both for crystalline silicate ([Navarro-Ruiz et al. 2014](#)) and amorphous silicate ([Navarro-Ruiz et al. 2015](#)), but they have not been confirmed experimentally yet.

Uncertainty of the H_2 formation rate on warm dust grains also has been discussed in PDRs illuminated by strong radiation from massive stars. Except for the absence of small dust grains, the environments are similar to debris disks. In such PDRs, [Habart et al. \(2011\)](#) ob-

servationally found that rotationally-excited H_2 is more abundant than the predictions of PDR models, suggesting that the H_2 production rate on warm dust grains needs to be higher than a typical value (e.g. Jura 1974). This result suggests that there is significant uncertainty in H_2 formation rates on warm dust grains.

As will be mentioned in Section 2.5, considering the uncertainty of T_{chem} , T_{chem} is changed as one of the model parameters in our PDR calculations.

2.5. Model Parameters

We summarize the model parameters in our models and show their parameter spaces. The model parameters are divided into ones related to the radiation field, the dust, gas components, the H_2 formation on the grain surface. The model parameters are tabulated in Table 2.

2.5.1. The Parameters Related to the Radiation Fields, $(\chi_{\text{co}}, \chi_{\text{oh}})$

As mentioned in Section 2.3, in order to investigate how the CO chemistry depends on radiation fields, the weak-FUV and strong-FUV models are considered. They are characterized by χ_{co} and χ_{oh} .

2.5.2. The Parameter Related to the Amount of Dust Grains, f_{dg}

The amount of dust grains is characterized by $\mathcal{N}_{\text{C}, \tau_{\text{mid}}=1}^{\text{fid}}$. We here estimate $\mathcal{N}_{\text{C}, \tau_{\text{mid}}=1}^{\text{fid}}$ from observation results of β Pictoris and 49 Ceti, which are examples of the stars having gas-poor and gas-rich debris disks, respectively. Since both the debris disks are almost edge-on, the observed column densities are comparable to those along the mid-plane. The total column density of species “A” integrated along the mid-plane is denoted by $\mathcal{N}(\text{A})$.

For β Pictoris, several authors derive the C^0 column densities from the $[\text{CI}] \ ^3P_1\text{--}^3P_0$ emission line (Higuchi et al. 2017; Cataldi et al. 2018) and 3P absorption lines (Roberge et al. 2000). Their values range from $\mathcal{N}(\text{C}^0) \sim 2 \times 10^{16}$ to $7 \times 10^{16} \text{ cm}^{-2}$. The C^+ column densities are estimated to be $\sim 2 \times 10^{16} - 12 \times 10^{16} \text{ cm}^{-2}$ from the $[\text{CII}] \ 158 \ \mu\text{m}$ emission line (Cataldi et al. 2014, 2018) and absorption lines (Roberge et al. 2006). The CO column densities are estimated to be $3 \times 10^{14} - 5 \times 10^{14} \text{ cm}^{-2}$ from emission lines (Higuchi et al. 2017) and $\sim 6 \pm 0.3 \times 10^{14} \text{ cm}^{-2}$ from absorption lines (Roberge et al. 2000). These observations suggest that $\mathcal{N}(\text{C}^0)$ is comparable to $\mathcal{N}(\text{C}^+)$, and $\mathcal{N}(\text{CO})$ is roughly two orders of magnitude smaller than $\mathcal{N}(\text{C}^0)$ and $\mathcal{N}(\text{C}^+)$. The carbon nucleus column density \mathcal{N}_{C} is estimated to be $\sim \mathcal{N}(\text{C}^0) + \mathcal{N}(\text{C}^+) \sim 10^{17} \text{ cm}^{-2}$. The spatial distribution of the dust surface area obtained

by HST observations of Heap et al. (2000) is fitted by Fernández et al. (2006). The mid-plane optical depth is about $\tau_{\text{mid}} \sim 10^{-2}$, where the fitting formula is integrated over $50 \text{ au} \leq R \leq 120 \text{ au}$, which is the gas extent of the best fit model in Cataldi et al. (2018). Finally, $\mathcal{N}_{\text{C}, \tau_{\text{mid}}=1}^{\beta\text{Pic}} \sim \mathcal{N}_{\text{C}}/\tau_{\text{mid}} \sim 10^{19} \text{ cm}^{-2}$ is obtained for β Pictoris.

For 49 Ceti, the C^0 and CO column densities are estimated to be $\mathcal{N}(\text{C}^0) \sim 2 \times 10^{18} \text{ cm}^{-2}$ (Higuchi et al. 2019) and $\mathcal{N}(\text{CO}) \sim 1.8 \times 10^{17} - 5.9 \times 10^{17} \text{ cm}^{-2}$ (Higuchi et al. 2020), respectively. The C^+ column density is not well constrained because only a lower limit of the C^+ mass, which is smaller than the CO mass, was obtained (Roberge et al. 2013). We however expect that \mathcal{N}_{C} is comparable to $\mathcal{N}(\text{C}^0)$ because $\mathcal{N}(\text{C}^+)$ should not be much larger than $\mathcal{N}(\text{C}^0)$ if all CO are formed through chemical reactions. The vertical optical depth estimated from the fractional luminosity is $\tau \sim 10^{-3}$ (Jura et al. 1993, 1998). Assuming that the aspect ratio of the dust distribution is ~ 0.1 , the mid-plane optical depth is $\tau_{\text{mid}} \sim 10^{-2}$. Finally, we obtain $\mathcal{N}_{\text{C}, \tau_{\text{mid}}=1}^{49\text{Ceti}} \sim 2 \times 10^{20} \text{ cm}^{-2}$ for 49 Ceti.

From $\mathcal{N}_{\text{C}, \tau_{\text{mid}}=1}^{\beta\text{Pic}} = 10^{19} \text{ cm}^{-2}$ and $\mathcal{N}_{\text{C}, \tau_{\text{mid}}=1}^{49\text{Ceti}} = 2 \times 10^{20} \text{ cm}^{-2}$, a fiducial value of $\mathcal{N}_{\text{C}, \tau_{\text{mid}}=1} = \mathcal{N}_{\text{C}}/\tau_{\text{mid}}$ is set to $\mathcal{N}_{\text{C}, \tau_{\text{mid}}=1}^{\text{fid}} = 2 \times 10^{19} \text{ cm}^{-2}$ ($\mathcal{N}_{\text{C}, \tau_{\text{mid}}=1}^{\beta\text{Pic}} = 0.5\mathcal{N}_{\text{C}, \tau_{\text{mid}}=1}^{\text{fid}}$, $\mathcal{N}_{\text{C}, \tau_{\text{mid}}=1}^{49\text{Ceti}} = 10\mathcal{N}_{\text{C}, \tau_{\text{mid}}=1}^{\text{fid}}$) because the behavior of the CO formation changes around $\mathcal{N}_{\text{C}, \tau_{\text{mid}}=1} \sim \mathcal{N}_{\text{C}, \tau_{\text{mid}}=1}^{\text{fid}}$ for weak-FUV and strong-FUV as will be shown in Section 3.

In this paper, instead of $\mathcal{N}_{\text{C}, \tau_{\text{mid}}=1}$, a normalized dust-to-gas mass ratio is used as the parameter indicating the amount of dust grains. Using Equation (7), one obtains

$$\frac{f_{\text{dg}}}{f_{\text{dg}, \text{fid}}} = \left(\frac{\mathcal{N}_{\text{C}, \tau_{\text{mid}}=1}}{\mathcal{N}_{\text{C}, \tau_{\text{mid}}=1}^{\text{fid}}} \right)^{-1}, \quad (9)$$

where $f_{\text{dg}, \text{fid}}$ is the dust-to-gas mass ratio at $\mathcal{N}_{\text{C}, \tau_{\text{mid}}=1} = \mathcal{N}_{\text{C}, \tau_{\text{mid}}=1}^{\text{fid}}$ and given by

$$f_{\text{dg}, \text{fid}}(a_{\text{min}}, a_{\text{max}}, Z) = 3 \times 10^{-3} \{Z^{-1} + 6.6 \times 10^{-3}\}^{-1} \times \left(\frac{a_{\text{min}}}{1 \ \mu\text{m}} \right)^{1/2} \left(\frac{a_{\text{max}}}{10 \ \mu\text{m}} \right)^{1/2} \quad (10)$$

where $n(a) \propto a^{-3.5}$ is used. We should note that although both f_{dg} and $f_{\text{dg}, \text{fid}}$ depend on a_{min} and a_{max} , the ratio $f_{\text{dg}}/f_{\text{dg}, \text{fid}}$ is independent of the size distribution for a given $\mathcal{N}_{\text{C}, \tau_{\text{mid}}=1}$.

To study how the amount of dust grains affects the thermal and chemical structures, the PDR calculations are performed with three different f_{dg} as listed in Table 2. For weak-FUV, since a typical f_{dg} is about $\sim 2f_{\text{dg}, \text{fid}}$ for β Pictoris, the cases with $(0.1f_{\text{dg}, \text{fid}}, f_{\text{dg}, \text{fid}}, 10f_{\text{dg}, \text{fid}})$

are considered. For strong-FUV, since a typical f_{dg} is about $\sim 0.1 f_{\text{dg, fid}}$, the cases with $(10^{-2} f_{\text{dg, fid}}, 0.1 f_{\text{dg, fid}}, f_{\text{dg, fid}})$ are considered.

2.5.3. The Parameters Related to the Gas Component, (n_{C}, Z)

The parameters associated with the gas component are n_{C} and metallicity Z . Given n_{C} and Z , the corresponding hydrogen nucleus number density is $n_{\text{H}} = n_{\text{C}}(\mathcal{A}_{\text{C}}Z)^{-1}$, where $\mathcal{A}_{\text{C}} = 1.32 \times 10^{-4}$ is the carbon elemental abundance of the gas for $Z = 1$ (Table 1). The hydrogen gas density is difficult to constrain in most debris disks observationally although there are some successful exceptions which will be described in Section 4.4.

Fiducial carbon nucleus number densities are defined as $n_{\text{C}} = 1.32 \times 10^2 \text{ cm}^{-3}$ for weak-FUV and $n_{\text{C}} = 1.32 \times 10^3 \text{ cm}^{-3}$ for strong-FUV. The debris disk around β Pictoris has a spatial extent of $\sim 70 \text{ au}$ in the best-fit model in Cataldi et al. (2018, also see Section 4.2.2). A mean density is $n_{\text{C}} \sim 10^{17} \text{ cm}^{-2}/70 \text{ au} \sim 100 \text{ cm}^{-3}$, which is comparable to the fiducial n_{C} for weak-FUV. For 49 Ceti, because the radial extent is $\sim 100 \text{ au}$, which corresponds to a cut-off radius of the surface density distribution (Hughes et al. 2018, also see Section 4.2.3), the mean density is $n_{\text{C}} \sim 2 \times 10^{18} \text{ cm}^{-2}/100 \text{ au} \sim 10^3 \text{ cm}^{-3}$, which is comparable to the fiducial n_{C} for strong-FUV. For comparison, the densities 10 times larger than the typical n_{C} are also considered for both the weak-FUV and strong-FUV models.

Next, we consider a range of the gas metallicity. The gas metallicity in debris disks depends on its origin. If the gas is a remnant of PPDs, the gas metallicity is expected not to be significantly different from the solar metallicity $Z = 1$. It is maximized when all the gas comes from the secondary processes; hydrogen is provided by photo-dissociation of H_2O outgassed from dust grains. In this case, the number of hydrogen nuclei becomes comparable to that of oxygen nuclei, and the gas metallicity reaches 1.6×10^3 since $\mathcal{A}_{\text{O}} = 3.2 \times 10^{-4}$ at $Z = 1$ (Table 1). In this paper, a range of $1 \leq Z \leq 10^3$ is considered.

2.5.4. The Parameter Related to the H_2 Formation on the Grain Surface, T_{chem}

In order to investigate how the uncertainty of the H_2 formation affects CO formation (Section 2.4.6), the cases with $T_{\text{chem}} = 300 \text{ K}$ and 10 K are considered. The fiducial case $T_{\text{chem}} = 300 \text{ K}$ leads to a moderate H_2 formation rate, corresponding to situations where chemisorption efficiently occurs on grains with plenty of surface defects (Le Bourlot et al. 2012). The cases with $T_{\text{chem}} = 10 \text{ K}$ give an upper limit of the H_2 formation rate. Other parameters T_{stick} and β are fixed to 464 K

and 1.5 , respectively, because the gas temperatures do not exceed $\sim 500 \text{ K}$ in most cases.

3. RESULTS

3.1. Overall Behaviors of the Models with the Solar Metallicity

In this section, we investigate how the results of the fiducial models ($n_{\text{C}} = 1.32 \times 10^2 \text{ cm}^{-3}$ for weak-FUV and $n_{\text{C}} = 1.32 \times 10^3 \text{ cm}^{-3}$ for strong-FUV) depend on the dust parameters ($f_{\text{dg}}/f_{\text{dg, fid}}, T_{\text{chem}}$) and incident FUV fluxes ($\chi_{\text{co}}, \chi_{\text{oh}}$). The gas metallicity is set to $Z = 1$.

We should note that the results with different a_{min} and a_{max} are not presented because our results are independent of both a_{min} and a_{max} as long as $f_{\text{dg}}/f_{\text{dg, fid}}$ and n_{C} remain unchanged. This is explained as follows. The grain-surface chemistry and photo-electric heating from dust grains are characterized by the total geometric cross section of dust grains $n_{\text{d}}\langle\pi a^2\rangle$. Equations (6) and (9) give

$$n_{\text{d}}\langle\pi a^2\rangle = \frac{n_{\text{C}}}{\mathcal{N}_{\text{C}, \tau_{\text{mid}}=1}} = \left(\frac{f_{\text{dg}}}{f_{\text{dg, fid}}}\right) \frac{n_{\text{C}}}{\mathcal{N}_{\text{C}, \tau_{\text{mid}}=1}^{\text{fid}}}, \quad (11)$$

where we use the fact that $Q_{\text{abs}} = 1$ because $Q_{\text{abs}} \sim 1$ for $a > 1 \mu\text{m}$. Equation (11) shows that $n_{\text{d}}\langle\pi a^2\rangle$ is controlled by n_{C} and $f_{\text{dg}}/f_{\text{dg, fid}}$. Since $\mathcal{N}_{\text{C}, \tau_{\text{mid}}=1}^{\text{fid}}$ is a given quantity, $n_{\text{d}}\langle\pi a^2\rangle$ does not depend on the size distribution of dust grains if n_{C} and $f_{\text{dg}}/f_{\text{dg, fid}}$ are fixed. Thus, the thermal and chemical processes related to dust grains, i.e., H_2 formation on dust grains and photo-electric heating, are independent of the size distribution for fixed n_{C} and $f_{\text{dg}}/f_{\text{dg, fid}}$.

The results are shown in Figure 2. In this paper, instead of the optical depth, N_{C} is used as a measure of the spatial coordinate, where N_{C} is the carbon nucleus column density integrated from the slab edge to a given position. In Figure 2, the maximum column densities are set to $N_{\text{C}} = 10^{17} \text{ cm}^{-2}$ for weak-FUV and $N_{\text{C}} = 2 \times 10^{18} \text{ cm}^{-2}$ for strong-FUV according to the observational constraints shown in Section 2.5.

3.1.1. Gas temperature

Figures 2a and 2b show that the gas temperatures increase with f_{dg} for both the weak-FUV and strong-FUV models because the photo-electric heating rate from dust grains, which is one of the dominant heating processes, increases in proportion to $f_{\text{dg}}/f_{\text{dg, fid}}$. A weak positive dependence of T on T_{chem} is attributed to enhancement of the heating rate owing to the H_2 formation on the grain surface.

Comparison between Figures 2a and 2b shows that the gas temperatures increase with χ_{co} because the photo-electric heating rate increases with χ_{co} .

parameter	weak-FUV	strong-FUV
FUV flux (CO, H ₂ , C ⁺) χ_{co}	1.4	31
FUV flux (OH) χ_{oh}	2.4	24
dust-to-gas mass ratio f_{dg}	$0.1f_{\text{dg, fid}}, f_{\text{dg, fid}}, 10f_{\text{dg, fid}}$	$0.01f_{\text{dg, fid}}, 0.1f_{\text{dg, fid}}, f_{\text{dg, fid}}$
gas density n_{C} [cm ⁻³]	$1.32 \times 10^2 \text{ cm}^{-3}, 1.32 \times 10^3 \text{ cm}^{-3}$	$1.32 \times 10^3 \text{ cm}^{-3}, 1.32 \times 10^4 \text{ cm}^{-3}$
the gas metallicity Z	1, 10, 10 ² , 10 ³	
T_{chem} [K] ⁽¹⁾	300, 10	

Table 2. ⁽¹⁾The energy barrier of chemisorption. List of the model parameters considered in the plane-parallel PDR calculations

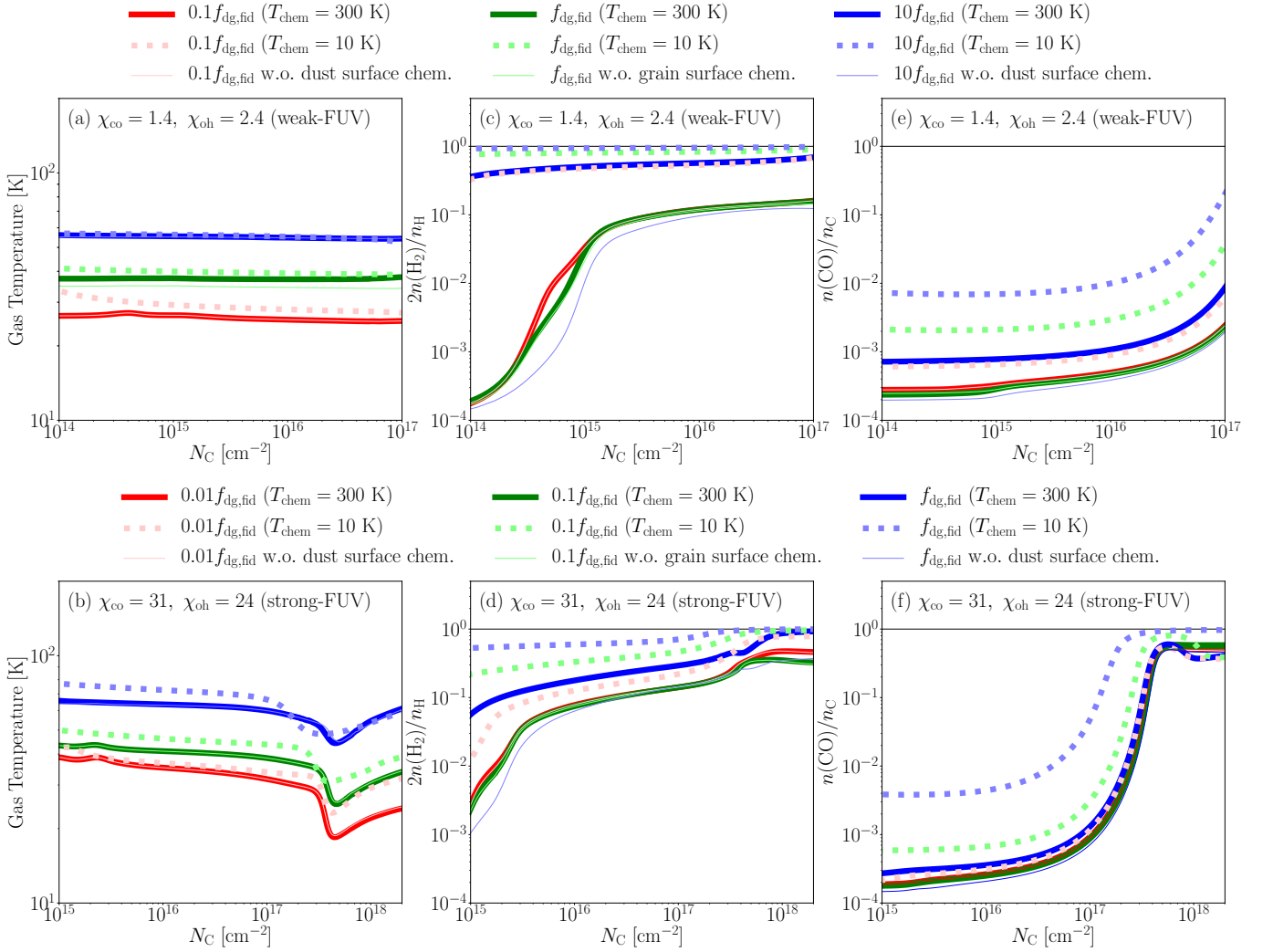


Figure 2. Results of the PDR calculations where the incident flux corresponds to the summation of ISRF and stellar radiation flux at a representative distance of 50 au from the central star. Profiles of the gas temperature (left column), $2n(\text{H}_2)/n_{\text{H}}$ (middle column), and $n(\text{CO})/n_{\text{C}}$ (right column) as a function of N_{C} . The top and bottom panels show the results for weak-FUV and strong-FUV models, respectively. The gas metallicity is fixed to $Z = 1$, and the gas densities are fixed to $n_{\text{C}} = 1.32 \times 10^2 \text{ cm}^{-3}$ for weak-FUV and $n_{\text{C}} = 1.32 \times 10^3 \text{ cm}^{-3}$ for strong-FUV. The colors represent f_{dg} which are $(0.1f_{\text{dg, fid}}, f_{\text{dg, fid}}, 10f_{\text{dg, fid}})$ for weak-FUV and $(0.01f_{\text{dg, fid}}, 0.1f_{\text{dg, fid}}, f_{\text{dg, fid}})$ for strong-FUV. The thick solid and dotted lines correspond to the results with $T_{\text{chem}} = 300 \text{ K}$ and 10 K , respectively. The thin solid line indicates the results without the H₂ formation on the grain surface.

3.1.2. Molecular Hydrogen

Before presenting the results, we introduce the analytic formation rate of H_2 on grain surfaces,

$$F_{\text{H}_2, \text{dust}} = 3 \times 10^{-3} R_{\text{H}_2, \text{ISM}} Z \left(\frac{f_{\text{dg}}}{f_{\text{dg}, \text{fid}}} \right) \sqrt{T} \kappa(T) n_{\text{H}} n(\text{H}) \quad (12)$$

(Le Bourlot et al. 2012), where Equation (11) is used, $R_{\text{H}_2, \text{ISM}} = 3 \times 10^{-17} \text{ cm}^3 \text{ s}^{-1}$ is a typical rate coefficient in the ISM (Jura 1974), and $\kappa(T)$ is the chemisorption efficiency⁵. Le Bourlot et al. (2012) derived

$$\kappa(T) = \frac{\alpha(T) \exp(-T_{\text{chem}}/T)}{1 + \alpha(T) \exp(-T_{\text{chem}}/T)}, \quad (13)$$

where $\alpha(T)$ and T_{chem} are defined in Section 2.4.6. For gas temperatures lower than $T_{\text{stick}} = 464 \text{ K}$, which is satisfied in all the cases shown in Figure 2, the H_2 formation rate is proportional to $\exp(-T_{\text{chem}}/T)$, and it depends sensitively on T .

First, the cases with $T_{\text{chem}} = 300 \text{ K}$ are considered. Although H_2 mainly forms on grain surfaces for the ISM, this may not be the case for debris disks because the H_2 formation rate is extremely small. In order to examine the contribution of the grain-surface chemistry to H_2 formation, we performed the additional PDR calculations where the grain-surface chemistry is switched off and plotted the results by the thin lines in the middle column of Figure 2. For $f_{\text{dg}} \leq f_{\text{dg}, \text{fid}}$ (weak-FUV) and $f_{\text{dg}} \leq 0.1 f_{\text{dg}, \text{fid}}$ (strong-FUV), there are almost no changes in the H_2 fractions with and without the grain-surface chemistry (Figures 2c and 2d), indicating that the grain-surface chemistry does not contribute to H_2 formation. In this case, H_2 is mainly formed in the gas phase, and the dominant chemical reaction is $\text{CH}^+ + \text{H} \rightarrow \text{H}_2 + \text{C}^+$, where CH^+ is formed by the radiative association between C^+ and H ⁶.

The H_2 formation rate of the grain-surface chemistry is enhanced in proportion to f_{dg} (Equation (12)) while the rate in the gas phase does not change. As shown

in Figures 2c and 2d, f_{dg} is high enough for H_2 to be formed mainly through the grain-surface chemistry when $f_{\text{dg}} = 10 f_{\text{dg}, \text{fid}}$ for weak-FUV and $f_{\text{dg}} = f_{\text{dg}, \text{fid}}$ for strong-FUV.

For $T_{\text{chem}} = 300 \text{ K}$, the H_2 fractions stay low level even after they increase rapidly around $\sim 10^{14} \text{ cm}^{-2}$ owing to self-shielding (Draine & Bertoldi 1996). This is because the H_2 formation rate is so low that the destruction reactions in the gas phase and H_2 photo-dissociation keep the H_2 fractions low.

As mentioned in Section 2.4.6, there is large uncertainty in H_2 formation on the warm dust grains with $T_{\text{gr}} \sim 100 \text{ K}$. A decrease in T_{chem} from 300 K to 10 K significantly enhances the H_2 fractions in Figures 2c and 2d because $\kappa(T)$ depends sensitively on T_{chem} . Considering the gas temperatures shown in Figures 2a and 2b, the H_2 formation rate increases by a factor of $\sim 1.6 \times 10^4$ at $T = 30 \text{ K}$ and $\sim 1.3 \times 10^2$ at $T = 60 \text{ K}$.

3.1.3. Carbon Monoxide, CO

First, the models with $T_{\text{chem}} = 300 \text{ K}$ are considered. Figures 2e and 2f show that $n(\text{CO})/n_{\text{C}}$ does not depend on f_{dg} significantly as long as $f_{\text{dg}} \leq f_{\text{dg}, \text{fid}}$ for both weak-FUV and strong-FUV. The CO fractions decrease with increasing χ_{co} because stronger FUV flux destroys CO more efficiently.

When f_{dg} is increased from $f_{\text{dg}, \text{fid}}$ to $10 f_{\text{dg}, \text{fid}}$, the weak-FUV models show that the CO fractions increase by a factor of 2 or 3.

Acceleration of the CO formation owing to H_2 is more significant for $T_{\text{chem}} = 10 \text{ K}$ than for $T_{\text{chem}} = 300 \text{ K}$ since a decrease in T_{chem} increases the H_2 fraction (Section 3.1.2). The CO fractions monotonically increase with f_{dg} .

The f_{dg} -dependence of the CO fractions disappears when the grain-surface chemistry is omitted from the PDR calculations. This clearly indicates that the enhancement of the CO fraction for larger f_{dg} is related to efficient H_2 formation on the grain surface.

How much H_2 is needed to accelerate CO formation? Comparing between the middle and right columns of Figure 2, one can see that H_2 fraction must be well above 0.1 for the CO fractions to increase by more than one order of magnitude. When the H_2 fraction is comparable to 0.1 as in the strong-FUV models with ($f_{\text{dg}} = 0.01 f_{\text{dg}, \text{fid}}$, $T_{\text{chem}} = 10 \text{ K}$) and ($f_{\text{dg}} = f_{\text{dg}, \text{fid}}$, $T_{\text{chem}} = 300 \text{ K}$), CO formation is not accelerated significantly.

In the deep interior $N_{\text{C}} > 5 \times 10^{16} \text{ cm}^{-2}$, the CO fractions increase owing to shielding effects, which will be discussed in Section 3.2.3.

3.2. CO Formation in H_2 -poor Environments

⁵ We should note that the Meudon code does not solve Equation (12) directly, but solves a set of rate equations considering chemisorbed hydrogen atoms and the dust size distribution (see Le Bourlot et al. 2012, for details). In addition to the chemisorbed H atoms, the Meudon code treats H_2 formation with physisorbed H atoms.

⁶ Especially for metal-poor environments, the so-called H^- channel is an important H_2 formation path (e.g., Sternberg et al. 2021). Additional PDR calculations were performed with chemical reactions associated with H^- , which had not been activated in the default setting of the Meudon code. The photo-detachment of H^- is computed directly from $\int \sigma_{\lambda} I_{\lambda} / h\nu d\lambda$ (Section 2.2), where the cross section obtained in Wishart (1979) is used while the Meudon code calculates it by using a fitting formula. We confirmed that the H^- channel does not affect the CO chemistry.

In Section 3, we show that the CO formation is independent of the amount of H_2 when H_2 formation is inefficient in situations where T_{chem} is high and/or f_{dg} is small. In this section, we investigate how CO forms in such H_2 -poor environment, and develop an analytic formula for the CO fraction that is applicable in a wide range of N_{C} in Sections 3.2.2 and 3.2.3.

3.2.1. Dependence of CO Fractions on Gas Metallicity

Figure 3 shows the spatial distributions of the CO fractions for various χ , n_{C} , and Z listed in Table 2. The dust-to-gas mass ratios are fixed to $f_{\text{dg}} = 0.1 f_{\text{dg, fid}}$ for weak-FUV and $f_{\text{dg}} = 0.01 f_{\text{dg, fid}}$ for strong-FUV, where the CO formation proceeds, regardless of H_2 (Figure 2).

We first focus on the CO fractions for $N_{\text{C}} \lesssim 10^{17} \text{ cm}^{-2}$. For given n_{C} and the FUV fluxes ($\chi_{\text{co}}, \chi_{\text{oh}}$), the CO fractions decrease with increasing Z . Since Z is changed keeping n_{C} constant, n_{H} decreases with increasing Z . The CO fractions thus decrease with decreasing n_{H} . This behavior has been pointed out by Higuchi et al. (2017); hydrogen is involved in CO formation.

Comparing between the panels of Figure 3, one can see that the CO fractions increase as n_{C} increases and/or χ_{co} decreases. This behavior was qualitatively expected because the CO formation rate will increase with increasing n_{C} and the CO destruction rate will decrease with decreasing χ_{co} .

For all the models shown in Figure 3, the CO fractions begin to increase in deep interiors owing to shielding effects, which will be investigated in Section 3.2.3.

3.2.2. An Analytical Formula for the CO Fraction

In this section, we develop an analytic formula for the CO fractions from the most important chemical reactions associated with CO formation of the H_2 -free gas in Figure 4. There are three main paths to form CO. At the high density limit (Equation (23)), the CO formation is intermediated mainly by OH (Path_{OH}). For lower densities, the dominant CO formation path depends on Z . At $Z \leq 10$, the CO formation is intermediated by CH^+ (Path_{CH⁺}). For higher Z , the CO formation proceeds without hydrogen as shown by the green arrows in Figure 4 (Path_{woH}).

The analytic formula taken into account all the chemical reactions shown in Figure 4 is complicated and is not useful. In Appendix A, we construct a fitting formula of the CO fraction based on Path_{OH}, which is dominated for higher densities, as follows:

$$\frac{n(\text{CO})_{\text{ana}}}{n_{\text{C}}} = \frac{\mathcal{A}_{\text{O}}}{\mathcal{A}_{\text{O, ism}}} (10^{-14} \eta^{1.8} + 6.0 \times 10^{-11} \eta), \quad (14)$$

where

$$\eta = n_{\text{H}} Z^{0.4} \chi^{-1.1}, \quad (15)$$

$\chi \equiv \sqrt{\chi_{\text{co}} \chi_{\text{oh}}}$, \mathcal{A}_{O} is the relative oxygen abundance with respect to hydrogen in the gas phase, and $\mathcal{A}_{\text{O, ism}} = 3.2 \times 10^{-4} Z$ corresponds to \mathcal{A}_{O} shown in Table 1.

We should note that Equation (14) is based on the chemical reactions in regions where shielding effects are not important. However, by considering the shielding effect in χ , we will show Equation (14) is applicable also in regions where shielding effects are effective in Section 3.2.3.

3.2.3. Application of the Analytical Formula to Regions Where Shielding Effects Work

The analytic formula $n(\text{CO})_{\text{ana}}$ at a given position depends on n_{H} , Z , and $\chi = \sqrt{\chi_{\text{co}} \chi_{\text{oh}}}$. Although n_{H} and Z are given locally, χ is determined by the column densities integrated from sources of light. The FUV radiation that destroys CO can be attenuated by dust grains, C^0 , CO, and H_2 . In debris disks, the dust extinction is negligible.

Which of C^0 , CO, and H_2 is more important for the shielding effects? In each shielding effect, one can define the critical column density at which χ_{co} is halved. Their critical densities are

$$\begin{aligned} N(\text{H}_2)_{\text{shld}} &\sim 4 \times 10^{20} \text{ cm}^{-2}, \\ N(\text{C}^0)_{\text{shld}} &\sim 4 \times 10^{16} \text{ cm}^{-2} \\ N(\text{CO})_{\text{shld}} &\sim 10^{14} \text{ cm}^{-2}. \end{aligned} \quad (16)$$

$N(\text{H}_2)_{\text{shld}}$ is given by the results in van Dishoeck & Black (1988); we derive the H_2 column density at which the shielding factor becomes 0.5 by the linear interpolation using Table 5 of their paper at $\log_{10} N(\text{CO}) = 0$ (also see Visser et al. 2009). $N(\text{C}^0)_{\text{shld}}$ is given by $(\ln 2) \alpha_{\text{C}}^{-1}$, where $\alpha_{\text{C}} = 1.777 \times 10^{-17} \text{ cm}^2$ is the cross section of photo-ionization of C^0 (Heays et al. 2017), because the shielding factor owing to C^0 is proportional to $\exp(-\alpha_{\text{C}} N(\text{C}^0))$. $N(\text{CO})_{\text{shld}}$ is taken from the CO column density at which the shielding factor is 0.5 at $\log_{10} N(\text{H}_2) = 0$ in Table 5 of Visser et al. (2009, also see Equation (21)).

Let us estimate the importance of the shielding effect owing to H_2 . Considering the abundance ratio between hydrogen and carbon, one finds that the H_2 column density is expressed as $N(\text{H}_2) = 3.8 \times 10^3 Z^{-1} N(\text{C}^0)$, where it is assumed that all hydrogen is in H_2 ($n(\text{H}_2) = n_{\text{H}}/2$) and all carbon is in C^0 ($n(\text{C}^0) = n_{\text{C}}$). By contrast, in order for the shielding effect owing to H_2 to be more important than the C^0 attenuation, $N(\text{H}_2)$ should be larger than $10^4 N(\text{C}^0)$, where the numerical factor 10^4 corresponds to $N(\text{H}_2)_{\text{shld}}/N(\text{C}^0)_{\text{shld}}$. This condition is not satisfied even for $Z = 1$, and the shielding effect owing to H_2 is not important compared with the C^0 attenuation. For simplicity, the shielding by H_2 is neglected

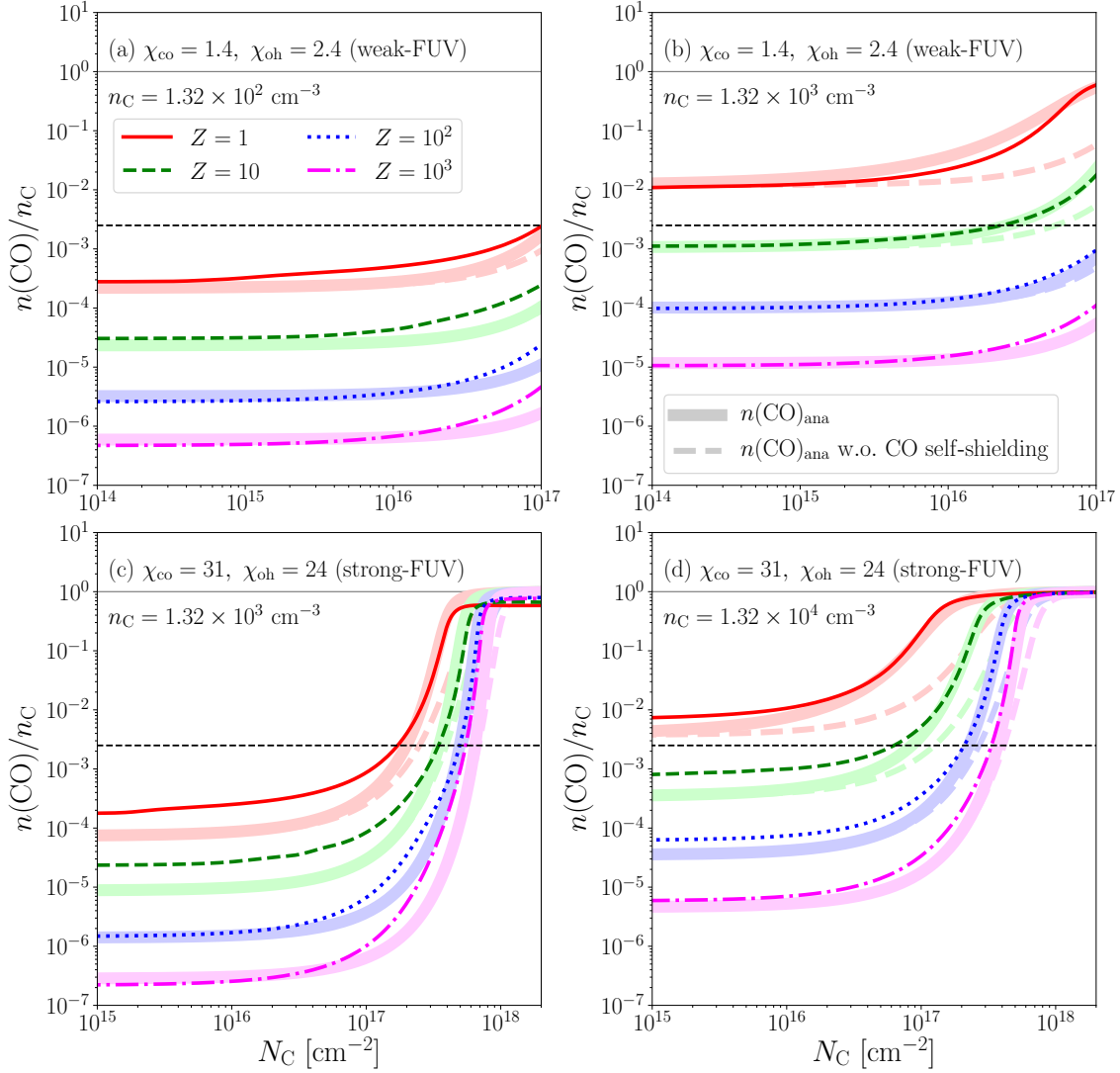


Figure 3. The CO fractions as a function of N_C for (a) weak-FUV ($n_C = 1.32 \times 10^2 \text{ cm}^{-3}$), (b) weak-FUV ($n_C = 1.32 \times 10^3 \text{ cm}^{-3}$), (c) strong-FUV ($n_C = 1.32 \times 10^3 \text{ cm}^{-3}$), and (d) strong-FUV ($n_C = 1.32 \times 10^4 \text{ cm}^{-3}$). The difference in the gas metallicities is shown by the red solid ($Z = 1$), green dashed ($Z = 10$), blue dotted ($Z = 10^2$), and magenta dot-dashed ($Z = 10^3$) lines. The horizontal black dashed lines indicate $(n(\text{CO})/n_C)_{\text{cri}}$ (Equation (25)). The thick lines with lighter colors show $n(\text{CO})_{\text{ana}}$ as a function of N_C taking into account both the C^0 and CO shielding effects. The dashed lines with lighter colors correspond to $n(\text{CO})_{\text{ana}}$ without the CO self-shielding effect.

in the analytic formula. We should note that the photo-dissociation rate may be overestimated in significantly shielded regions with $N(\text{H}_2) > N(\text{H}_2)_{\text{shld}}$.

In debris disks, C^0 and CO contribute mainly to a decrease in χ_{co} . The problem is that the C^0 and CO fractions both depend on local χ_{co} , which depends on their column densities. In this section, we construct a procedure to determine the spatial distributions of $n(\text{C}^0)$, $n(\text{CO})$, and χ_{co} consistently.

Before presenting a way to evaluate the shielding effects, we should mention about the analytic formulae for $n(\text{CO})$ and $n(\text{C}^0)$. The analytic formula for $n(\text{CO})$ shown in Equation (14) is not applicable directly to a

situation where carbon nuclei are mostly in CO because $n(\text{CO})_{\text{ana}}$ increases without limit as η increases. To address this issue, Equation (14) is simply modified so that $n(\text{CO})_{\text{ana}}$ approaches n_C smoothly in $\eta \rightarrow \infty$ as follows:

$$\frac{n(\text{CO})_{\text{ana}}}{n_C} = \left[1 + \left\{ \frac{\mathcal{A}_O}{\mathcal{A}_{O,\text{ism}}} (10^{-14} \eta^{1.8} + 6.0 \times 10^{-11} \eta) \right\}^{-1} \right]^{-1} \quad (17)$$

This modification may be ad hoc, but it predicts the CO fractions consistent with those obtained from the PDR calculations as will be shown in Figure 3.

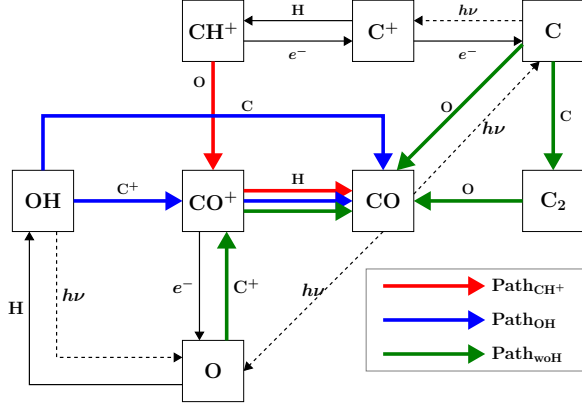


Figure 4. The most important reactions to form CO in the H_2 -free gas. The red and blue arrows show the CO formation paths intermediated by CH^+ and OH, respectively. The green arrows correspond to the CO formation paths not associated with hydrogen. The photo-dissociation of OH and CO and photo-ionization of C are shown by the dashed arrows. The chemical reaction rate coefficients are summarized in Table 6.

An analytic formula for the C^0 fraction is presented. The C^0 fraction is determined by the balance between photo-ionization of C^0 and radiative recombination of C^+ (Kamp & Bertoldi 2000) as follows:

$$\frac{n(\text{C}^0)_{\text{ana}}}{n_{\text{C}} - n(\text{CO})_{\text{ana}}} = \frac{2\xi + 1 - \sqrt{1 + 4\xi}}{2\xi}, \quad (18)$$

where the denominator $n_{\text{C}} - n(\text{CO})_{\text{ana}}$ guarantees that the sum of the C^0 , C^+ , and CO number densities is equal to n_{C} , and ξ is the ratio of the recombination to the ionization coefficients that is given by

$$\begin{aligned} \xi &\equiv \frac{k_{\text{rec}}(n_{\text{C}} - n(\text{CO})_{\text{ana}})}{\alpha_{\text{C}}\chi_{\text{co}}F_{\text{H}}} \\ &= \chi_{\text{co}}^{-1} \left(\frac{n_{\text{C}} - n(\text{CO})_{\text{ana}}}{11 \text{ cm}^{-3}} \right) \left(\frac{T}{100 \text{ K}} \right)^{-0.82}. \end{aligned} \quad (19)$$

We confirmed that Equation (18) reproduced the C^0 fractions obtained from the PDR calculations.

The normalized FUV flux χ_{co} is expressed in terms of the unattenuated value $\chi_{\text{co,thin}}$ as follows:

$$\chi_{\text{co}} = \chi_{\text{co,thin}} f_{\text{shield}}(N(\text{C}^0)_{\text{ana}}, N(\text{CO})_{\text{ana}}), \quad (20)$$

where f_{shield} corresponds to the shielding factor, which depends on the C^0 and CO column densities ($N(\text{C}^0)_{\text{ana}}$ and $N(\text{CO})_{\text{ana}}$) computed from $n(\text{C}^0)_{\text{ana}}$ and $n(\text{CO})_{\text{ana}}$, respectively. As the shielding factor, we adopt the following expression,

$$f_{\text{shld}} = e^{-\alpha_{\text{C}}N(\text{C}^0)_{\text{ana}}} \left[1 + \left(\frac{N(\text{CO})_{\text{ana}}}{10^{14} \text{ cm}^{-2}} \right)^{0.6} \right]^{-1}, \quad (21)$$

where the first factor on the right-hand side corresponds to the C^0 attenuation, and the second factor is a fitting function of the self-shielding factor at $N(\text{H}_2) = 0$ tabulated in Visser et al. (2009).

The spatial distributions of χ_{co} , $n(\text{C}^0)_{\text{ana}}$, and $n(\text{CO})_{\text{ana}}$ are determined consistently in an iterative manner by using Equations (17), (18), and (20).

It is useful to derive n_{H} required to produce a specific value of the CO fraction. In the high density limit where Path_{OH} is dominated, since the second term in the right-hand side of Equation (14) is negligible, Equation (14) is solved for n_{H} as follows:

$$\begin{aligned} n_{\text{H,req}} &= 6 \times 10^7 \text{ cm}^{-3} Z^{-0.4} \chi^{1.1} \\ &\times \left(\frac{\mathcal{A}_{\text{O}}}{\mathcal{A}_{\text{O,ism}}} \right)^{-0.56} \left(\frac{n(\text{CO})}{n_{\text{C}}} \right)^{0.56}, \end{aligned} \quad (22)$$

which is valid when

$$n_{\text{H,req}} > 5.3 \times 10^4 \text{ cm}^{-3} Z^{-0.4} \chi^{1.1}. \quad (23)$$

Equation (22) is rewritten as

$$\begin{aligned} n_{\text{C,req}} &= 8 \times 10^3 \text{ cm}^{-3} Z^{0.6} \chi^{1.1} \\ &\times \left(\frac{\mathcal{A}_{\text{O}}}{\mathcal{A}_{\text{O,ism}}} \right)^{-0.56} \left(\frac{n(\text{CO})}{n_{\text{C}}} \right)^{0.56}, \end{aligned} \quad (24)$$

which corresponds to the carbon nucleus density required to reproduce a specific value of $n(\text{CO})/n_{\text{C}}$. From Equation (24), an important conclusion can be drawn that $n(\text{CO})/n_{\text{C}}$ decreases with increasing Z for fixed n_{C} and χ . In other words, the upper limit of the CO fraction is obtained at $Z = 1$.

3.2.4. Comparison of the CO Fractions with Those Predicted from the Analytical Formula

Figure 3 compares the results of the PDR calculations with the predictions from the analytic formula. $n(\text{CO})_{\text{ana}}$ reproduces the spatial profiles of $n(\text{CO})$ reasonably well from the unattenuated regions ($N_{\text{C}} \ll 10^{17} \text{ cm}^{-2}$) to the shielded regions ($N_{\text{C}} \gtrsim 10^{17} \text{ cm}^{-2}$) for all the parameter sets.

For lower n_{C} shown in Figures 3a and 3c, the CO fractions begin to increase around $N_{\text{C}} \sim 10^{16-17} \text{ cm}^{-2}$, regardless of Z and χ . By contrast, Figures 3b and 3d show that the CO fractions with $Z = 1$ begin to increase at lower N_{C} . This comes from the fact that CO self-shielding only works if the CO fraction is high enough; otherwise, C^0 attenuation becomes more important.

A critical CO fraction above which CO self-shielding effect works is given by

$$\left(\frac{n(\text{CO})}{n_{\text{C}}} \right)_{\text{cri}} \sim \frac{N(\text{CO})_{\text{shld}}}{N(\text{C}^0)_{\text{shld}}} \sim 3 \times 10^{-3}. \quad (25)$$

The horizontal dashed lines in Figure 3 correspond to $(n(\text{CO})/n_{\text{C}})_{\text{cri}}$. In order to illustrate the effect of the CO self-shielding in Figure 3, we overplot the profiles of $n(\text{CO})_{\text{ana}}$ without considering the CO self-shielding effect in Equation (21) by the thick dashed lines. It is clearly seen that the CO self-shielding effect increases the CO fractions at $N_{\text{C}} < N(\text{C}^0)_{\text{shld}}$ only when $n(\text{CO})$ exceeds $n(\text{CO})_{\text{cri}}$.

The importance of C^0 attenuation in CO formation has been pointed out by Kral et al. (2019).

3.3. Parameter Survey

In Section 3.2, we developed the analytic formula which reproduces the results of the PDR calculations reasonably well when the H_2 fraction is too small to affect the CO formation. By contrast, in Section 3.1, we found that the models with lower T_{chem} and/or higher f_{dg} yield a sufficient amount of H_2 to accelerate the CO formation. In this section, we investigate how the CO fractions depend on f_{dg} , T_{chem} , and N_{C} for various n_{C} , Z , and χ_{co} .

3.3.1. The CO Fractions at $N_{\text{C}} = 10^{17} \text{ cm}^{-2}$

First, we investigate the CO fractions at $N_{\text{C}} = 10^{17} \text{ cm}^{-2}$, which is the mid-plane column density inferred from the observational results of β Pictoris (Section 2.5). At this column density, CO is not shielded by C^0 attenuation significantly while CO self-shielding can work if the CO fraction is sufficiently high (Section 3.2.4). For reference, we also investigate the CO fractions at $N_{\text{C}} = 10^{17} \text{ cm}^{-2}$ for strong-FUV. The top and middle panels of Figure 5 show the CO fractions as a function of $f_{\text{dg}}/f_{\text{dg, fid}}$ for various n_{C} , T_{chem} , and χ_{co} . Overall, as T_{chem} decreases and/or f_{dg} increases, the CO fractions increase and deviate from the predictions from the analytic formula.

First, we investigate the results with $T_{\text{chem}} = 300 \text{ K}$ (Figures 5a, 5c, 5e, and 5g). There is a critical $f_{\text{dg}}/f_{\text{dg, fid}}$ ($(f_{\text{dg}}/f_{\text{dg, fid}})_{\text{cri}}$) above which the CO formation is accelerated. $(f_{\text{dg}}/f_{\text{dg, fid}})_{\text{cri}}$ depends on the parameters. For the fiducial weak-FUV models ($n_{\text{C}} = 1.32 \times 10^2 \text{ cm}^{-3}$), $(f_{\text{dg}}/f_{\text{dg, fid}})_{\text{cri}}$ is around 1, regardless of Z (Figure 5a). For the high-density weak-FUV models ($n_{\text{C}} = 1.32 \times 10^3 \text{ cm}^{-3}$), $(f_{\text{dg}}/f_{\text{dg, fid}})_{\text{cri}}$ depends on Z (Figure 5c). The $Z \geq 10^2$ models show acceleration of the CO formation at $f_{\text{dg}}/f_{\text{dg, fid}} = 1$ while $(f_{\text{dg}}/f_{\text{dg, fid}})_{\text{cri}}$ is around 1 for $Z \leq 10$.

The f_{dg} dependence of the CO fractions for the fiducial strong-FUV models ($n_{\text{C}} = 1.32 \times 10^3 \text{ cm}^{-3}$) is similar to that for the high-density weak-FUV models ($n_{\text{C}} = 1.32 \times 10^3 \text{ cm}^{-3}$) (see Figures 5c and 5e); enhancement of the CO fractions is seen only for $Z \gtrsim 10^2$

when $f_{\text{dg}}/f_{\text{dg, fid}}$ is increased from 0.1 to 1. For the high-density strong-FUV model ($n_{\text{C}} = 1.32 \times 10^4 \text{ cm}^{-3}$), $(f_{\text{dg}}/f_{\text{dg, fid}})_{\text{cri}} \sim 0.1$ for all Z .

The short summary is that $(f_{\text{dg}}/f_{\text{dg, fid}})_{\text{cri}} \sim 1$ for $n_{\text{C}} = 1.32 \times 10^2 \text{ cm}^{-3}$, $(f_{\text{dg}}/f_{\text{dg, fid}})_{\text{cri}} \sim 0.1$ for $n_{\text{C}} = 1.32 \times 10^4 \text{ cm}^{-3}$, and the models with $n_{\text{C}} = 1.32 \times 10^3 \text{ cm}^{-3}$ show the intermediate behavior where $(f_{\text{dg}}/f_{\text{dg, fid}})_{\text{cri}}$ takes values between 0.1 and 1 depending on Z . The dependence of χ_{co} on $(f_{\text{dg}}/f_{\text{dg, fid}})_{\text{cri}}$ appears to be weak.

A decrease in T_{chem} reduces $(f_{\text{dg}}/f_{\text{dg, fid}})_{\text{cri}}$ significantly. Figures 5b, 5d, 5f, and 5h show that $(f_{\text{dg}}/f_{\text{dg, fid}})_{\text{cri}} < 0.1$ for weak-FUV and $(f_{\text{dg}}/f_{\text{dg, fid}})_{\text{cri}} \sim 10^{-2}$ for strong-FUV. The CO fractions monotonically increase with $f_{\text{dg}}/f_{\text{dg, fid}}$ for most cases.

We should note that increases in the CO fractions appear to saturate for the weak-FUV models with ($n_{\text{C}} = 1.32 \times 10^2 \text{ cm}^{-3}$, $f_{\text{dg}} \geq f_{\text{dg, fid}}$, $Z > 1$, $T_{\text{chem}} = 10 \text{ K}$) and ($n_{\text{C}} = 1.32 \times 10^3 \text{ cm}^{-3}$, $f_{\text{dg}} \geq f_{\text{dg, fid}}$, $Z > 10$, $T_{\text{chem}} = 10 \text{ K}$). This is because the H_2 fractions are close to unity in these models, and the enhancement of the H_2 formation rate does not lead to further acceleration of the CO fractions.

The CO fractions at $N_{\text{C}} = 10^{17} \text{ cm}^{-2}$ are affected by CO self-shielding when the CO fractions exceed $(n(\text{CO})/n_{\text{C}})_{\text{cri}}$ (Equation (25)), which is shown by the horizontal dashed black lines. When $n(\text{CO})/n_{\text{C}} > (n(\text{CO})/n_{\text{C}})_{\text{cri}}$, a small increase in $n(\text{CO})/n_{\text{C}}$ for $N_{\text{C}} < 10^{17} \text{ cm}^{-2}$ results in a large increase in $N(\text{CO})/N_{\text{C}}$ at $N_{\text{C}} = 10^{17} \text{ cm}^{-2}$. This effect is clearly seen in Figures 5b and 5d.

What chemical reactions contribute to the acceleration of the CO formation? We found that vibrationally excited H_2 (hereafter H_2^*) plays an important role. As a result, different reaction paths to CO are activated than the chemical reactions shown in Figure 4. It starts from $\text{C}^+ + \text{H}_2 \rightarrow \text{CH}^+ + \text{H}$ which is known to be endothermic by $\sim 4300 \text{ K}$. The internal energy of H_2^* is available to overcome its energy barrier. The reaction between C^+ and H_2^* with $v > 0$ proceeds at almost the Langevin collision rate ($k_{\text{cp, h2}^*} = 1.6 \times 10^{-9} \text{ cm}^3 \text{ s}^{-1}$) (Hierl et al. 1997).

The efficiency of the mechanism is investigated in Zanchet et al. (2013b) and Herrez-Aguilar et al. (2014). In PDRs of the ISM, the importance of H_2^* was also pointed out in many references (Agundez et al. 2010; Goicoechea et al. 2016; Joblin et al. 2018; Veselinova et al. 2021; Goicoechea & Roncero 2022).

How much H_2^* is required to accelerate CO formation? Figure 6 shows the scatter plots of $2N(\text{H}_2^*)/N_{\text{H}}$ versus a boost factor f_{boost} , which is defined as the CO

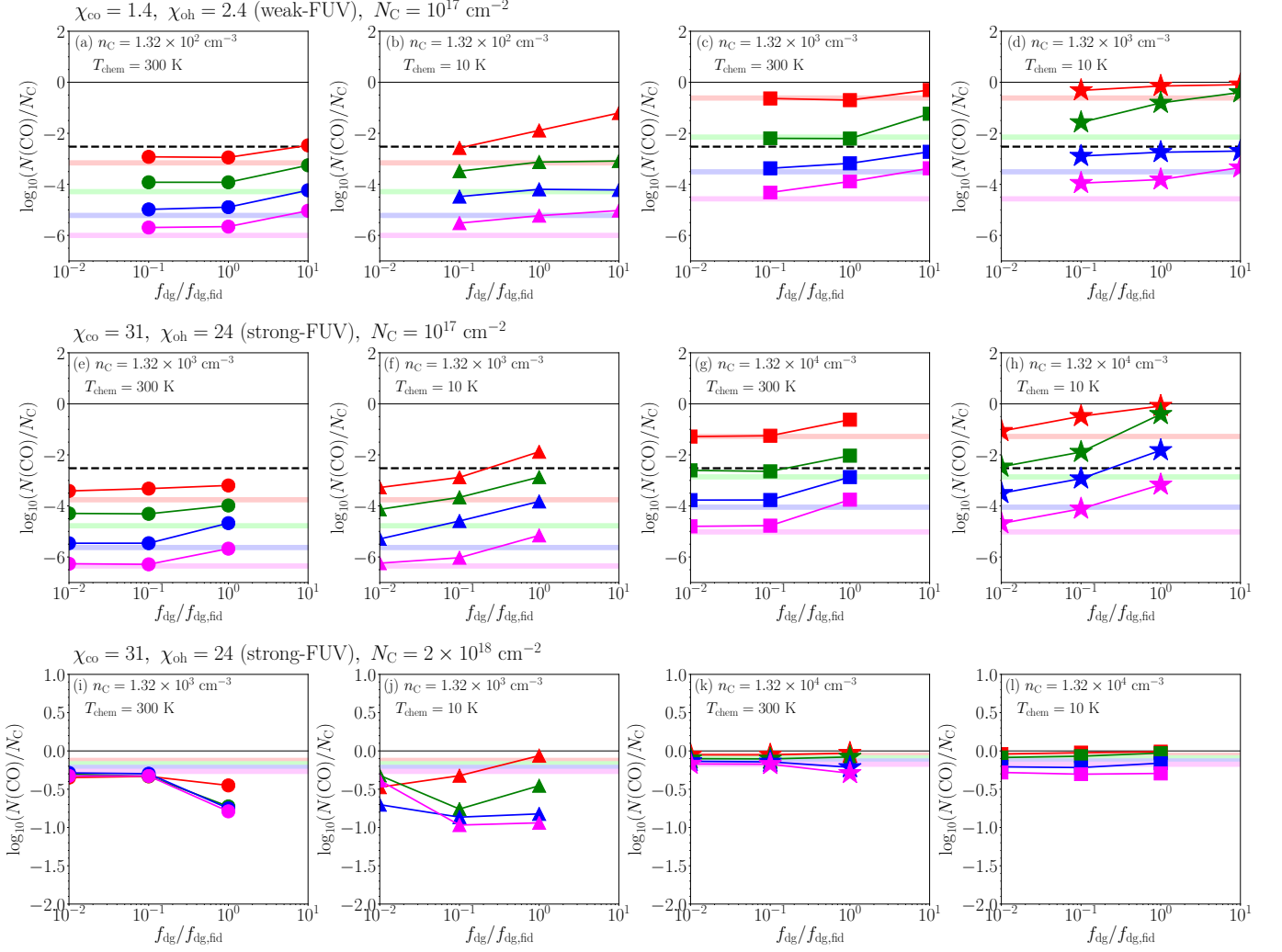


Figure 5. CO column density ratios $N(\text{CO})/N_{\text{C}}$ as a function of $f_{\text{dg}}/f_{\text{dg,fid}}$ for (*top panels*) the weak-FUV models with $N_{\text{C}} = 10^{17} \text{ cm}^{-2}$, (*middle panels*) the strong-FUV models with $N_{\text{C}} = 10^{17} \text{ cm}^{-2}$, and (*bottom panels*) the strong-FUV models with $N_{\text{C}} = 2 \times 10^{18} \text{ cm}^{-2}$. The results with 2×2 combinations of $n_{\text{C}} = (1.32 \times 10^2 \text{ cm}^{-3}, 1.32 \times 10^3 \text{ cm}^{-3})$ and $T_{\text{chem}} = (300 \text{ K}, 10 \text{ K})$ for weak-FUV and $n_{\text{C}} = (1.32 \times 10^3 \text{ cm}^{-3}, 1.32 \times 10^4 \text{ cm}^{-3})$ and $T_{\text{chem}} = (300 \text{ K}, 10 \text{ K})$ for strong-FUV. In each panel, the color represents the gas metallicities, (red) $Z = 1$, (green) $Z = 10$, (blue) $Z = 10^2$, and (magenta) $Z = 10^3$. The horizontal thick lines correspond to the predictions from $n(\text{CO})_{\text{ana}}$ with four different Z ($Z = 1, 10, 10^2, 10^3$). The horizontal dashed black lines show the critical CO fraction $(n(\text{CO})/n_{\text{C}})_{\text{cri}}$ (Equation (25)) above which the CO is shielded mainly by self-shielding.

fraction divided by that at the H_2 -poor environments where only f_{dg} is changed to $0.1f_{\text{dg,fid}}$ for weak-FUV and $0.01f_{\text{dg,fid}}$ for strong-FUV, keeping the other parameters unchanged.

Figure 6 show that f_{boost} is correlated with $2N(\text{H}_2^*)/N_{\text{H}}$ for both weak-FUV and strong-FUV, indicating that H_2^* accelerates the CO formation. f_{boost} is larger than unity only when $2N(\text{H}_2^*)/N_{\text{H}}$ exceeds a critical H_2^* fraction of $\sim 10^{-7}$ although there are large scatters.

The critical H_2^* fraction can be roughly understood as follows. A necessary condition affecting the CO formation by H_2^* is that the reaction rate of $\text{C}^+ + \text{H}_2^* \rightarrow \text{CH}^+ + \text{H}$ must be larger than that of

$\text{C}^+ + \text{H} \rightarrow \text{CH}^+ + h\nu$. The condition becomes

$$n(\text{H}_2^*) > n(\text{H}_2^*)_{\text{cri}} = \frac{k_{\text{cp,h}}}{k_{\text{cp,h2}^*}} n_{\text{H}} \sim 3 \times 10^{-8} \left(\frac{T}{50 \text{ K}} \right)^{-0.42} n_{\text{H}}, \quad (26)$$

where $k_{\text{cp,h}} = 2.29 \times 10^{-17} (T/300)^{-0.42} \text{ cm}^3 \text{ s}^{-1}$ is the reaction rate of $\text{C}^+ + \text{H} \rightarrow \text{CH}^+ + h\nu$. Figures 6 show that $2N(\text{H}_2^*)/N_{\text{H}} > 2n(\text{H}_2^*)_{\text{cri}}/n_{\text{H}}$ can distinguish whether to accelerate the CO formation or not.

The correlation between f_{boost} and $2N(\text{H}_2^*)/N_{\text{H}}$ depends on Z ; the models with lower Z tend to show larger f_{boost} at a fixed $2N(\text{H}_2^*)/N_{\text{H}}$. This is because for smaller Z , the efficient formation of CH^+ activates more reac-

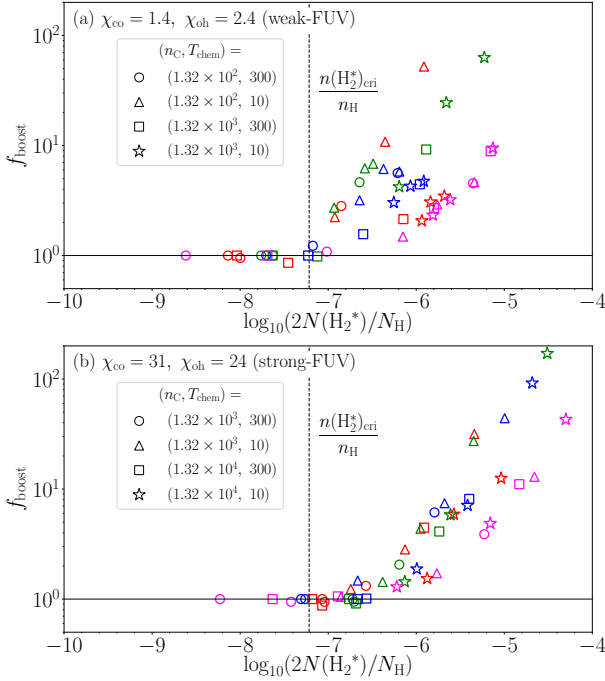


Figure 6. Scatter plots of f_{boost} versus $2N(\text{H}_2^*)/N_{\text{H}}$, where f_{boost} shows the degree of the enhancement of the CO fraction owing to H_2^* for (a) weak-FUV and (b) strong-FUV. The column densities are measured at $N_{\text{C}} = 10^{17} \text{ cm}^{-2}$. The ranges of the parameters $(n_{\text{C}}, T_{\text{chem}}, Z, f_{\text{dg}})$ are shown in Table 2. The data points are distinguished by n_{C} , T_{chem} , and Z . The shapes of the markers represent the difference in $(n_{\text{C}}, T_{\text{chem}})$. The colors of the markers represent different gas metallicities, (red) $Z = 1$, (green) 10, (blue) 10^2 , and (magenta) 10^3 . The data points with different f_{dg} are illustrated without distinction, but $2N(\text{H}_2^*)/N_{\text{H}}$ increase with f_{dg} . The vertical dashed black lines correspond to $2n(\text{H}_2^*)_{\text{cri}}/n_{\text{H}}$ defined in Equation (26).

tion pathways involved by hydrogen to produce CO since n_{H} increases with decreasing Z at a given n_{C} .

3.3.2. The CO Fractions at $N_{\text{C}} = 2 \times 10^{18} \text{ cm}^{-2}$

We investigate the CO fractions for strong-FUV at $N_{\text{C}} = 2 \times 10^{18} \text{ cm}^{-2}$, which is the mid-plane column density inferred from the observational results of 49 Ceti (Section 2.5). At this column density, CO is shielded significantly.

Interestingly the CO fractions at $N_{\text{C}} = 2 \times 10^{18} \text{ cm}^{-2}$ show the opposite f_{dg} -dependence from that at $N_{\text{C}} = 10^{17} \text{ cm}^{-2}$. For $T_{\text{chem}} = 300 \text{ K}$, increases in f_{dg} reduce the CO fractions (Figures 5i and 5k). The production of CH^+ through the reaction between C^+ and H_2^* does not contribute to the CO formation because the C^0 attenuation makes the C^+ fractions extremely low. That is why efficient formation of H_2 no longer promotes the CO formation. Conversely, the presence of H_2 negatively affects CO formation. In the chemical network shown in

Figure 4, an increase in the amount of H_2 reduces the amount of available H atoms, leading to a decrease in the CO formation rate.

A similar behavior is seen for $T_{\text{chem}} = 10 \text{ K}$. As long as $f_{\text{dg}} \leq 0.1f_{\text{dg, fid}}$, increasing f_{dg} reduces the amount of CO. When f_{dg} is increased from $0.1f_{\text{dg, fid}}$ to $f_{\text{dg, fid}}$, the CO fractions turn to increase in Figures 5j and 5l. This is because most hydrogen exists as H_2 for $f_{\text{dg}} = f_{\text{dg, fid}}$. The chemical reactions shown in Figure 4 no longer work, and different chemical reactions associated with H_2 become important to form CO.

4. DISCUSSION

4.1. Predictions of the Spatial Distributions of CO in a Disk Structure

The Meudon PDR code is not designed to investigate the chemical and thermal structure of disks. However, in Section 3.2, we developed the numerical procedure to determine the CO fractions on the basis of the findings of the plane-parallel PDR calculations. In this section, we present the method to derive the spatial distributions of $n(\text{C}^0)_{\text{ana}}$ and $n(\text{CO})_{\text{ana}}$ in a given disk structure using a similar method as shown in Section 3.2.3.

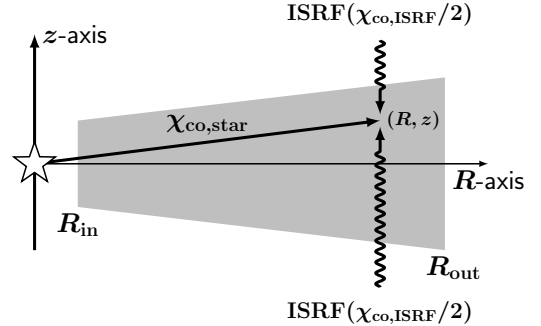


Figure 7. Schematic picture of our setting where the three rays are considered.

Figure 7 shows the disk structure considered in this paper. The disk extends from $R = R_{\text{in}}$ to R_{out} , where the cylindrical coordinate (R, z) is used and the central star locates at the origin. The density distribution of carbon nuclei is denoted as $n_{\text{C}}(R, z)$, and Z and f_{dg} are assumed to be uniform throughout the disk. At a certain position (R, z) , the local radiation field is determined by the three rays, the stellar radiation that penetrates the disk from the inner edge to (R, z) and the ISRF that propagates vertically from above and below the disk toward (R, z) .

Applying Equation (20) into the cases with the disk geometry, one obtains $\chi_{\text{co}}(R, z)$ as follows:

$$\begin{aligned} \chi_{\text{co}}(R, z) = & \chi_{\text{co,star}} \left(\frac{\sqrt{R^2 + z^2}}{r_0} \right)^{-2} f_{\text{shield},r}(R, z) \\ & + \frac{\chi_{\text{co,ISRF}}}{2} f_{\text{shield},+z}(R, z) \\ & + \frac{\chi_{\text{co,ISRF}}}{2} f_{\text{shield},-z}(R, z), \end{aligned} \quad (27)$$

where $\chi_{\text{co,star}}$ and $\chi_{\text{co,ISRF}}$ are the normalized unattenuated FUV fluxes of the stellar radiation at a reference radius of $r_0 = 50$ au and the ISRF, respectively. The geometrical dilution is considered in the first term on the right-hand side of Equation (27). A shielding factor is defined for each of the three rays; $f_{\text{shield},r}$ is the shielding factor of the stellar radiation, and $f_{\text{shield},+z}$ ($f_{\text{shield},-z}$) is the shielding factor of the ISRF coming from below (above) the disk. They are computed using Equation (21), but the column densities $N(\text{CO})_{\text{ana}}$ and $N(\text{C}^0)_{\text{ana}}$ are computed by integrating $n(\text{CO})_{\text{ana}}$ and $n(\text{C}^0)_{\text{ana}}$ along the corresponding rays, respectively.

The normalized FUV flux χ_{oh} is given by

$$\chi_{\text{oh}}(R, z) = \chi_{\text{oh,star}} \left(\frac{\sqrt{R^2 + z^2}}{r_0} \right)^{-2}, \quad (28)$$

where $\chi_{\text{oh,star}}$ is the normalized unattenuated FUV flux of the stellar radiation at $r_0 = 50$ au. Shielding effects are not effective in χ_{oh} as mentioned in Section 2.3

From Equations (18), (17), (27), and (28), $n(\text{C}^0)_{\text{ana}}(R, z)$, $n(\text{CO})_{\text{ana}}(R, z)$, and $\chi_{\text{co}}(R, z)$ are determined consistently in an iterative manner.

4.2. Comparison with Observations

Our analytical model shown in Section 4.1 is applied to the debris disks around β Pictoris and 49 Ceti in Sections 4.2.2 and 4.2.3, respectively.

Although $n(\text{C}^0)_{\text{ana}}(R, z)$ and $n(\text{CO})_{\text{ana}}(R, z)$ are obtained throughout the disk, additional PDR calculations are conducted at various radii along the mid-plane considering the stellar radiation and vertical ISRF. There are two reasons for this. One is to verify whether $n(\text{C}^0)_{\text{ana}}$ and $n(\text{CO})_{\text{ana}}$ reproduce the results of the PDR calculations with $T_{\text{chem}} = 300$ K. The other is to investigate how the H_2 formation accelerated by setting $T_{\text{chem}} = 10$ K affects the CO formation. Section 4.2.1 will describe how the PDR calculations are conducted taking into account the disk geometry.

4.2.1. PDR Calculations Using Disk Geometry and Structure

In the PDR calculation at ($R = R_i, z = 0$), supposing that $I_{\text{star}}(\lambda)$ is the stellar radiation intensity and

	low-density	high-density
$n_{\text{C,mid0}} [\text{cm}^{-3}]^{(1)}$	75	190
$\mathcal{N}_{\text{C}} [\text{cm}^{-2}]^{(2)}$	4×10^{16}	10^{17}
$\mathcal{N}_{\text{C}\perp} [\text{cm}^{-2}]^{(3)}$	1.8×10^{16}	4.4×10^{16}
$f_{\text{dg}}/f_{\text{dg,fid}}$	5.0	2.0

Table 3. List of the model parameters for β Pictoris. ⁽¹⁾The mid-plane carbon nucleus number densities at $R = 50$ au. ⁽²⁾The mid-plane carbon nucleus column densities integrated from R_{in} to R_{out} . ⁽³⁾The vertical carbon nucleus number densities with $Z = 1$.

$I_{\text{ISRF}}(\lambda)$ is the ISRF intensity, the mean intensity $J(\lambda)$ at $(R_i, 0)$ is given by

$$\begin{aligned} J(\lambda) = & I_{\text{star}}(\lambda) W(R_i) f_{\text{shield},r}(R_i, 0) \\ & + I_{\text{ISRF}}(\lambda) f_{\text{shield},+z}(R_i, 0) \end{aligned} \quad (29)$$

for $\lambda \leq 1100$ Å, where $W(R_i)$ is the geometrical dilution factor at $R = R_i$, and we use the fact that $f_{\text{shield},-z}(R_i, 0) = f_{\text{shield},+z}(R_i, 0)$. For the spectrum with $\lambda > 1100$ Å, the shielding factors in Equation (29) are set to unity.

For each R_i , we perform the PDR calculation with $n_{\text{C}}(R_i, 0)$, Z , $f_{\text{dg}}/f_{\text{dg,fid}}$, and the radiation field shown in Equation (29). Since the geometrical dilution and shielding effects are already taken into account in the incident radiation, the chemical abundances at the optically thin limit ($N_{\text{C}} = 10^{14} \text{ cm}^{-2}$) are considered as those at the position $(R_i, 0)$.

4.2.2. β Pictoris

On the basis of the disk models shown in Cataldi et al. (2018), we here consider a ring with a uniform carbon nucleus vertical column density. With the C^0 and C^+ line data (Cataldi et al. 2014, 2018), Cataldi et al. (2018) derive the best fit parameters of $R_{\text{in}} = 50$ au and $R_{\text{out}} = 120$ au. The stellar parameters of the central star adopted here are the same as those of the A5V star shown in Section 2.3. The scale height is $h(R) = c_s(R)/\Omega(R)$, where c_s is the sound speed with the constant temperature $T = 75$ K and $\Omega(R) = \sqrt{G1.75M_{\odot}/R^3}$.

Since $\mathcal{N}_{\text{C}} \sim 10^{17} \text{ cm}^{-2}$ for β Pictoris (Section 2.5), an average mid-plane carbon nucleus number density is estimated to be $\sim \mathcal{N}_{\text{C}}/(R_{\text{out}} - R_{\text{in}}) \sim 100 \text{ cm}^{-3}$. In order to investigate how the CO fractions depend on the mid-plane density, we consider two different values of $n_{\text{C,mid0}} = n_{\text{C}}(R_{\text{in}}, 0)$ at the inner edge, $n_{\text{C,mid0}} = 75 \text{ cm}^{-3}$ (low-density model) and $n_{\text{C,mid0}} = 190 \text{ cm}^{-3}$ (high-density model) as listed in Table 3.

The radial distribution of the mid-plane density is given by

$$n_C(R, 0) = 75 \text{ cm}^{-3} \left(\frac{n_{C, \text{mid}0}}{75 \text{ cm}^{-3}} \right) \left(\frac{R}{50 \text{ au}} \right)^{-3/2}. \quad (30)$$

where the mean molecular weight μ is assumed to be spatially constant.

The mid-plane column densities \mathcal{N}_C integrated from $R = R_{\text{in}}$ to R_{out} for both the models are shown in Table 3. They correspond to the minimum and maximum values of the observed C^0 column densities multiplied by two (Higuchi et al. 2017; Cataldi et al. 2018), where the factor two comes from the contribution from C^+ .

The vertical column density $\mathcal{N}_{C\perp}$ is determined by multiplying $n_C(R, 0)$ by the scale height, which depends on T and μ . Although μ depends on the chemical state of the species, for simplicity, we assume that all gases are neutral atoms, and μ is given by $1.27(1 + 6.6 \times 10^{-3}Z)/(1 + 5.5 \times 10^{-4}Z)$. Even when the gas is fully molecular, our results do not change significantly because μ will be about a factor of two larger and the vertical column density decreases by about 30%.

Referring to Equation (9), the dust-to-gas mass ratio is expressed in terms of \mathcal{N}_C and τ_{mid} as follows:

$$\frac{f_{\text{dg}}}{f_{\text{dg}, \text{fid}}} = \left(\frac{\mathcal{N}_C}{2 \times 10^{17} \text{ cm}^{-2}} \right)^{-1} \left(\frac{\tau_{\text{mid}}}{10^{-2}} \right). \quad (31)$$

From Equation (31), the dust-to-gas mass ratios are given by $f_{\text{dg}}/f_{\text{dg}, \text{fid}} = 5.0$ for the low-density model and 2.0 for the high-density model, where $\tau_{\text{mid}} = 10^{-2}$ is used (Table 3).

Using the analytical model presented in Section 4.1, the spatial distribution of χ_{co} is obtained. Figures 8a and 8b show χ_{co} at the mid-plane as a function of R . χ_{co} is almost constant because the ISRF gives dominant contribution in most radii except near the inner edge. Since the vertical column density for the high-density model is around $N(\text{C}^0)_{\text{shld}}$, χ_{co} is slightly attenuated. By contrast, χ_{oh} at the mid-plane decreases with R owing to the geometrical dilution.

Before showing the results of the PDR calculations, we present the approximate formula of the predictions from the analytic formula. Equation (23) can be rewritten as $n_{C, \text{req}} > 7Z^{0.6}\chi^{-1.1} \text{ cm}^{-3}$. Since $n_C \sim 100 \text{ cm}^{-3}$ and $\chi \sim O(1)$, Equation (24) is valid for $Z \lesssim 10^2$. Equating the mid-plane density and the density required to produce a given CO fraction (Equation (24)), the CO fraction is expected to be

$$\left(\frac{n(\text{CO})}{n_C} \right)_{\beta \text{Pic}} = 10^{-4} \left(\frac{n_{C, \text{mid}0}}{75 \text{ cm}^{-3}} \right)^{1.8} \left(\frac{R}{50 \text{ au}} \right)^{-0.7} \times Z^{-1.1} \chi_{\text{co}}^{-1} \left(\frac{\mathcal{A}_O}{\mathcal{A}_{O, \text{ism}}} \right), \quad (32)$$

where Equation (28) is used for χ_{oh} , and χ_{co} is the attenuated local value. Integrating $n(\text{CO})$ over the disk extent with Equations (30) and (32), one obtains the predicted mid-plane CO column density,

$$\mathcal{N}(\text{CO})_{\beta \text{Pic}} = 3 \times 10^{12} \text{ cm}^{-2} \left(\frac{n_{C, \text{mid}0}}{75 \text{ cm}^{-3}} \right)^{2.8} \times Z^{-1.1} \langle \chi_{\text{co}}^{-1} \rangle \left(\frac{\mathcal{A}_O}{\mathcal{A}_{O, \text{ism}}} \right), \quad (33)$$

where $\langle \chi_{\text{co}}^{-1} \rangle$ is the average of χ_{co}^{-1} weighted by $R^{-2.2}$ over the disk extent.

The PDR calculations are conducted at four radii, 50 au, 75 au, 100 au, and 120 au.

Firstly, the cases with $Z = 1$ are considered. The results of the PDR calculations of the low-density and high-density models are shown in Figures 8c and 8d, respectively. For $T_{\text{chem}} = 300 \text{ K}$, the radial profiles of $n(\text{CO})/n_C$ are consistent with the predictions from the analytic model (Section 4.1) for both the models because H_2 formation is inefficient. Although $f_{\text{dg}}/f_{\text{dg}, \text{fid}}$ is slightly larger than unity, the effect of excited H_2 is limited as shown in Figure 5a.

When T_{chem} is decreased from 300 K to 10 K, the H_2 formation rate increases by about four orders of magnitude at $T \sim 40 \text{ K}$, making a large amount of hydrogen nuclei being molecular. As a result, H_2^+ increases the CO fraction by about an order of magnitude in both the models (Figures 8c and 8d). This is consistent with what we found in Figure 5b.

The mid-plane column densities of C^0 and CO integrated from $R = R_{\text{in}}$ to R are shown in Figures 8e and 8f as a function of R . After a rapid increase in $N(\text{CO})$ near the inner edge, they become almost constant outside from $R \sim 75 \text{ au}$. This clearly shows that the CO mid-plane column densities are determined near the inner edge, and CO in the outer disk does not contribute to the total column density.

In order to compare our results with the observational results, the mid-plane column densities of C^+ , C^0 , and CO integrated from $R = R_{\text{in}}$ to R_{out} are shown as a function of T_{chem} in Figure 9a. The C^0 column densities of the low- and high-density models are both consistent with the observational results, and do not depend on T_{chem} .

The CO column densities increase as the mid-plane gas density increases and/or T_{chem} decreases. The high-density models produce about an order of magnitude larger CO column densities than the low-density model for all T_{chem} . This comes from the fact that $\mathcal{N}(\text{CO}) \propto n_{C, \text{mid}0}^{2.8}$ (Equation (33)). The contribution of the attenuation of χ_{co} to an increase in $\mathcal{N}(\text{CO})$ is limited since the vertical column density $\mathcal{N}_{C\perp}$ is comparable to or

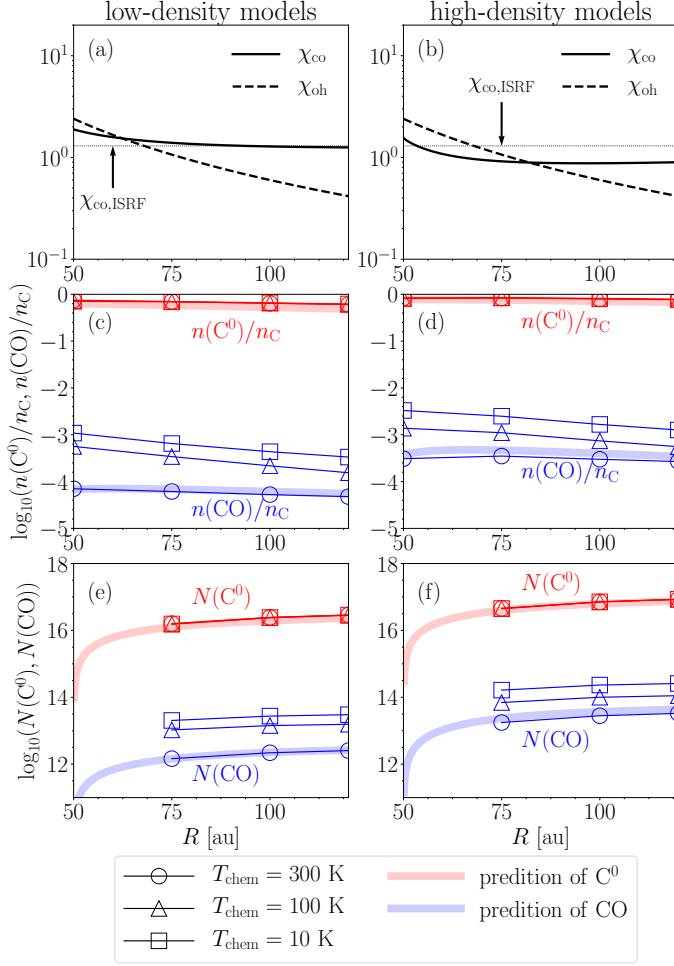


Figure 8. Results of the PDR calculations with $Z = 1$ for β Pictoris. As the stellar radiation field, A5V star is adopted. The left and right columns show the results of the low-density and high-density models, respectively. (*Top panels*) The normalized UV fluxes (solid) χ_{co} and (dashed) χ_{oh} . The horizontal dotted lines correspond to $\chi_{\text{co,ISRF}}$. (*Middle panels*) The radial distributions of (red) $n(\text{C}^0)/n_{\text{C}}$ and (blue) $n(\text{CO})/n_{\text{C}}$. The circles, triangles, and boxes correspond to the results for $T_{\text{chem}} = 300$ K, 100 K, and 10 K, respectively. The C^0 and CO fractions predicted from the analytic model (Section 4.1) are shown by the light red and blue solid lines, respectively. (*Bottom panels*) The radial column densities of (red) atomic carbon and (blue) CO integrated from the inner edge (50 pc) to R as a function of R .

smaller than $N(\text{C}^0)_{\text{shld}}$ (Table 3). The CO column density of the high-density model with $T_{\text{chem}} = 300$ K does not reach the lower limit of the observational constraints (Higuchi et al. 2017). If T_{chem} is lower than 100 K, the high-density models yield the CO column density comparable to the observational constraints.

The Z dependence of $\mathcal{N}(\text{CO})$ is shown in Figure 9b. For the fiducial models ($T_{\text{chem}} = 300$ K), $\mathcal{N}(\text{CO})$ decreases with increasing Z , roughly following the pre-

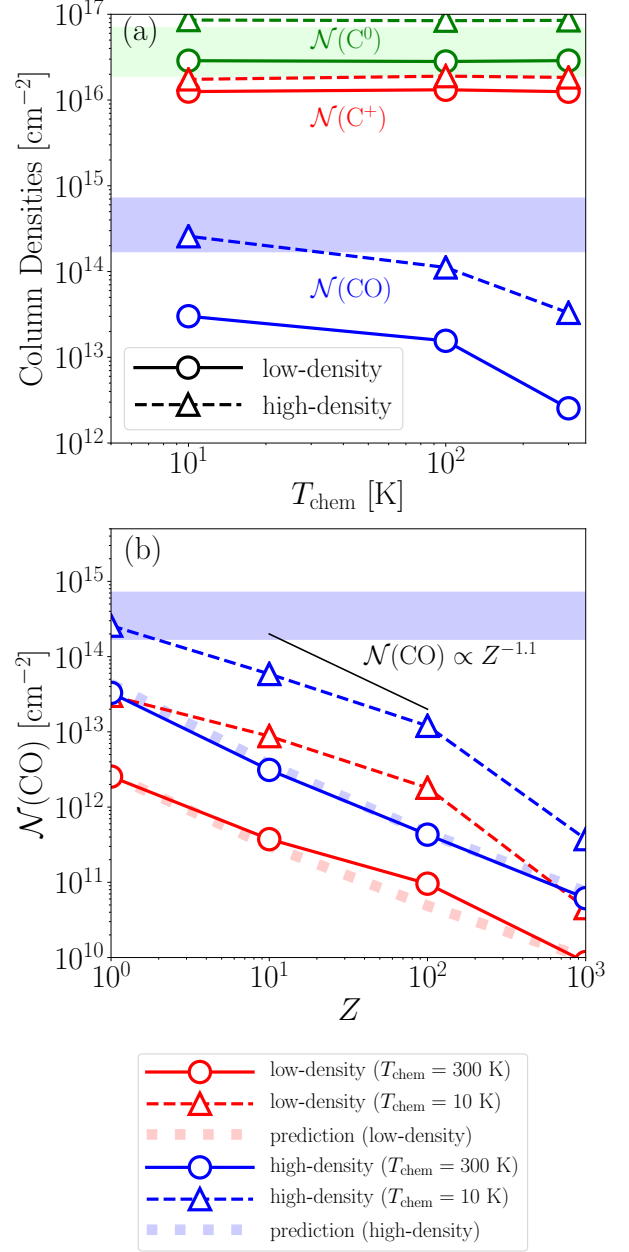


Figure 9. Results of the PDR calculations for β Pictoris. (a) The mid-plane column densities of (red) C^+ , (green) C^0 , and (blue) CO along the mid-plane as a function of T_{chem} for (circles) the low- and (triangles) high-density models with $Z = 1$. The green and blue rectangle regions indicate the observational constraints on the C^0 and CO column densities obtained from Higuchi et al. (2017); Cataldi et al. (2018) and Higuchi et al. (2017), respectively. (b) The mid-plane CO column densities as a function of Z for (red) the low- and (blue) high-density models. The circles and triangles show the results with $T_{\text{chem}} = 300$ K and $T_{\text{chem}} = 10$ K, respectively. The red and blue thick dashed lines correspond to the predictions from the analytic model (Section 4.1) with $T_{\text{chem}} = 300$ K and 10 K, respectively. The blue rectangle region is the same as that in Panel (a). As a reference, $\mathcal{N}(\text{CO}) \propto Z^{-1.1}$ is plotted (Equation (32)).

	low-density	high-density
$n_{\text{C,mid0}} [\text{cm}^{-3}]^{(1)}$	4.9×10^2	2.0×10^3
$\mathcal{N}_{\text{C}} [\text{cm}^{-2}]^{(2)}$	8.4×10^{17}	3.3×10^{18}
$\mathcal{N}_{\text{C}\perp} [\text{cm}^{-2}]^{(3)}$	8.2×10^{16}	3.5×10^{17}
$f_{\text{dg}}/f_{\text{dg,fid}}$	0.24	0.06

Table 4. List of the model parameters for 49 Ceti. ⁽¹⁾The mid-plane carbon nucleus number densities at $R = R_{\text{c}}/2 = 60$ au. ⁽²⁾The mid-plane carbon nucleus column densities integrated from the inner edge to infinity. ⁽³⁾The vertical carbon nucleus number densities with $Z = 1$ at $R = 60$ au.

dictions from Equation (33). When T_{chem} decreases to 10 K, $\mathcal{N}(\text{CO})$ is increased by an order of magnitude, keeping the Z dependence almost unchanged (also see Figure 5b). Figure 9b shows that metallicities larger than $Z = 1$ cannot reproduce the observational CO column densities even when the H_2 formation is enhanced by decreasing T_{chem} .

4.2.3. 49 Ceti

Following Hughes et al. (2017) and Higuchi et al. (2019), we adopt the disk model which has a power-law distribution with the inner edge at $R_{\text{in}} = 20$ au and with a exponential cut-off at $R = R_{\text{c}}$,

$$\mathcal{N}_{\text{C}\perp}(R) \propto \left(\frac{R}{R_{\text{c}}}\right)^{-\gamma} \exp\left[-\left(\frac{R}{R_{\text{c}}}\right)^{2-\gamma}\right], \quad (34)$$

where $R_{\text{in}} = 20$ au, $\gamma = -0.5$, and $R_{\text{c}} = 140$ au are the best fit parameters. The outer edge of the disk R_{out} is at infinity. The scale height is $h(R) = c_{\text{s}}(R)/\Omega$, where c_{s} is the sound speed with $T = 23 \text{ K}(R/100 \text{ au})^{-1/2}$ and $\Omega = \sqrt{GM_{\text{star}}/R^3}$, where M_{star} is the central star mass (Hughes et al. 2018, also see Table 5).

As discussed in Section 2.5, a typical mid-plane number density of carbon nuclei is given by $\sim 10^3 \text{ cm}^{-3}$, where $\mathcal{N}_{\text{C}} \sim 10^{18} \text{ cm}^{-2}$ is divided by the disk extent $R_{\text{c}} - R_{\text{in}}$. We consider two different values of the mid-plane carbon nucleus density at $R = R_{\text{c}}/2$, $n_{\text{C,mid0}} = 4.9 \times 10^2 \text{ cm}^{-3}$ (low-density model) and $n_{\text{C,mid0}} = 2.0 \times 10^3 \text{ cm}^{-3}$ (high-density model).

The mid-plane density is given by

$$n_{\text{C}}(R, 0) = 5.6 \times 10^2 \text{ cm}^{-3} \left(\frac{n_{\text{C,mid0}}}{4.9 \times 10^2 \text{ cm}^{-3}}\right) \times \left(\frac{R}{60 \text{ au}}\right)^{-3/4} \exp\left[-\left(\frac{R}{140 \text{ au}}\right)^{2.5}\right] \quad (35)$$

where μ is assumed to be spatially constant. The corresponding mid-plane column densities are listed in Table 4. The high-density model gives the mid-plane column

density comparable to or slightly larger than that predicted in Higuchi et al. (2019). As in the case of β Pictoris, the vertical column densities are determined by assuming all the gas is neutral atomic, and the values with $Z = 1$ at $R = 60$ au are listed in Table 4.

Substituting \mathcal{N}_{C} into Equation (31) gives $f_{\text{dg}}/f_{\text{dg,fid}} = 0.24$ for the low-density models and 0.06 for the high-density models, where $\tau_{\text{mid}} = 10^{-2}$ is used. Since $f_{\text{dg}}/f_{\text{dg,fid}}$ is much lower than unity, the acceleration of the CO formation owing to H_2^+ is not effective (Section 3.3.1).

	SSUV	WSUV
$M_{\text{star}} [M_{\odot}]^{(1)}$	2.1	2.0
$T_{\text{eff}} [\text{K}]^{(2)}$	10,000	9,000
$\log_{10} g^{(3)}$	4.5	4.3

Table 5. ⁽¹⁾ Stellar mass. ⁽²⁾ Effective temperature. ⁽³⁾ Surface gravity. The stellar models of SSUV and WSUV are taken from Hughes et al. (2008) and Roberge et al. (2013), respectively. In both models, the metallicities $[\text{M}/\text{H}]$ are assumed to be the solar one.

Different stellar parameters are used in the literature (Chen et al. 2006; Hughes et al. 2008; Montesinos et al. 2009; Roberge et al. 2013). Among the different stellar models, the two extreme stellar models that provide the smallest and largest $\chi = \sqrt{\chi_{\text{co}}\chi_{\text{oh}}}$ are considered. The stellar parameters of these models are summarized in Table 5. The strong and weak stellar UV models are called SSUV and WSUV, respectively.

Equating Equations (35) and Equation (24), one obtains the expected CO fraction,

$$\begin{aligned} \left(\frac{n(\text{CO})}{n_{\text{C}}}\right)_{49\text{Ceti}} &= 5.2 \times 10^{-4} \left(\frac{n_{\text{C,mid0}}}{490 \text{ cm}^{-3}}\right)^{1.8} \left(\frac{R}{60 \text{ au}}\right)^{0.62} \\ &\times Z^{-1.1} \chi_{\text{co}}^{-1} \left(\frac{\chi_{\text{oh}}}{\chi_{\text{oh,SSUV}}}\right)^{-1} \left(\frac{\mathcal{A}_{\text{O}}}{\mathcal{A}_{\text{O,ism}}}\right) \\ &\times \exp\left[-1.8 \left(\frac{R}{R_{\text{c}}}\right)^{2.5}\right], \end{aligned} \quad (36)$$

where $\chi_{\text{oh,SSUV}}$ shows χ_{oh} of the SSUV model.

Models SSUV (WSUV) with the lower and higher mid-plane densities are called SSUV_{low} (WSUV_{low}) and SSUV_{high} (WSUV_{high}), respectively.

First, the low-density models are focused on. Figures 10a and 10b show the radial distributions of the normalized UV fluxes for models WSUV_{low} and SSUV_{low}, respectively. Since the C^0 fractions are smaller for SSUV owing to the stronger FUV flux, χ_{co} decreases more slowly for SSUV_{low} than for WSUV_{low}. As a result, more outer parts of the disk is exposed to intense FUV

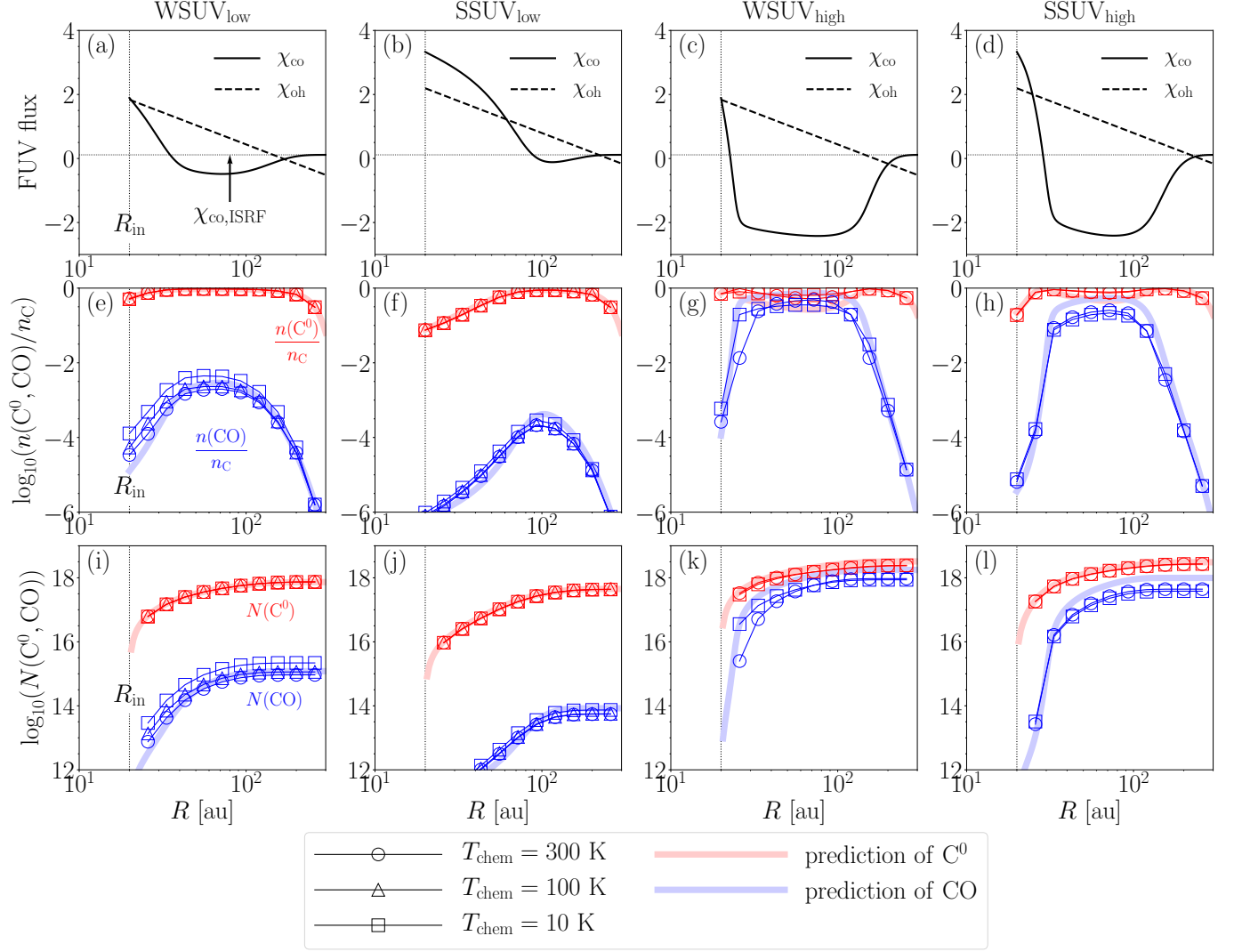


Figure 10. The same as Figure 8 but for 49 Ceti. The vertical dashed lines show the position of the disk inner edge $R_{\text{in}} = 20$ au.

radiation for SSUV_{low}. The FUV fluxes χ_{co} take minimum values in $R \sim 60$ au for WUV_{low} and in $R \sim 10^2$ au for SUV_{low}, and then increases to $\sim \chi_{\text{co,ISRF}}$ around $R \sim 200$ au. For WSUV_{low}, the vertical attenuation of χ_{co} is clearly seen in $40 \text{ au} < R < 200$ au because $\mathcal{N}_{\text{C},\perp}$ is larger than $N(\text{C}^0)_{\text{shld}}$ (Table 4).

The radial profiles of the C^0 and CO fractions in the low-density models with are shown in Figures 10e and 10f. For $T_{\text{chem}} = 300$ K, both the models clearly show that CO forms efficiently only in the region where the stellar radiation flux is low because $(n(\text{CO})/n_{\text{C}})$ is in proportion to χ_{co}^{-1} . Their radial distributions agree with the predictions from the analytic model (Section 4.1).

A decrease in T_{chem} does not affect the CO fractions significantly, compared with the results with β Pictoris (Figures 10e and 10f). The CO fractions are increased only by a factor of 2 or 3. This comes from the fact

that $f_{\text{dg}}/f_{\text{dg,fd}}$ for 49 Ceti is more than one order of magnitude smaller than that for β Pictoris. Roughly speaking, the inner (outer) regions dominated by the stellar radiation (the vertical ISRF) correspond to the strong-FUV (weak-FUV) models at $N_{\text{C}} \sim 10^{17} \text{ cm}^{-2}$. As seen in the first and middle panels of Figure 5, when $f_{\text{dg}} < 0.24 f_{\text{dg,fd}}$, the existence of H_2^+ increases the CO fractions only by a factor of 2 or 3.

When the mid-plane density increases, the behaviors of the CO fractions change significantly. The stellar radiation in the wavelength range of χ_{co} is almost attenuated in very inner regions even for model SSUV_{high}. Since the vertical column density $\mathcal{N}_{\text{C},\perp} = 3.5 \times 10^{17} \text{ cm}^{-2}$ at $R = 60$ au (Table 4) is much larger than $N(\text{C}^0)_{\text{shld}}$, the vertical attenuation of the ISRF is significant in $30 \text{ au} < R < 200$ au (Figures 10c and 10d).

Figures 10g and 10h show that both the high-density models yield large amounts of CO where χ_{co} is almost attenuated. The CO fractions in the attenuated regions are almost independent of T_{chem} . This is consistent with the results shown in Section 3.3.2. In a such attenuated region, $\text{C}^+ + \text{H}_2^* \rightarrow \text{CH}^+ + \text{H}$ does not accelerate the CO formation because of depletion of C^+ . We should note that the CO fractions slightly decrease with decreasing T_{chem} in the attenuated regions because the H atoms available for the CO chemistry shown in Figure 4 are reduced by enhancement of the H_2 formation (Section 3.3.2).

The bottom panels of Figures 10 show the radial distributions of $N(\text{C}^0)$ and $N(\text{CO})$ integrated from the inner edge to R . Increases in the CO column densities are saturated around the peak radius of $n(\text{CO})$. Thus, \mathcal{N}_{C} is determined in the amount of CO inside the peak radius of $n(\text{CO})$.

The obtained C^+ , C^0 , and CO column densities integrated along the mid-plane are compared with the observational results in Figure 11a for $Z = 1$. The low-density models show that the CO fractions does not reach the observed values for both the stellar models. By contrast, the high-density models produce sufficient amounts of CO to explain the observational results. We thus expect that there is a best solution to explain the observed CO column densities in $4.9 \times 10^2 \text{ cm}^{-3} < n_{\text{C},\text{mid}0} < 2.0 \times 10^3 \text{ cm}^{-3}$ (Table 4). For reference, we conducted additional PDR calculations with $n_{\text{C},\text{mid}0} = 1.2 \times 10^3 \text{ cm}^{-3}$ ($\mathcal{N}_{\text{C}} = 2 \times 10^{18} \text{ cm}^{-2}$). The mid-plane density is between those in the low-density and high-density models. Figure 11a show that a best solution is located in $1.2 \times 10^3 \text{ cm}^{-3} < n_{\text{C},\text{mid}0} < 2.0 \times 10^3 \text{ cm}^{-3}$, and both $\mathcal{N}(\text{C}^0)$ and $\mathcal{N}(\text{CO})$ of a best solution will be consistent with the observational results.

The Z dependence of $\mathcal{N}(\text{CO})$ is shown in Figure 11b. For all the models, the CO column densities decrease with increasing Z as $\mathcal{N}(\text{CO}) \propto Z^{-1.1}$, and are consistent with the predictions from Equation (36). Figure 11b shows that $\text{WSUV}_{\text{high}}$ ($\text{SSUV}_{\text{high}}$) provides $\mathcal{N}(\text{CO})$ consistent with the observed CO column densities if $1 < Z < 10$ ($Z \sim 1$). This suggests that if the gas is secondary-origin ($Z \sim 10^3$), the CO column densities cannot be explained only by steady-state chemical reactions.

4.3. Uncertainty of the H_2 Formation on Dust Grains

One of the main results of this paper is that the CO formation is affected strongly by T_{chem} , which is one of the uncertain parameters in the ER mechanism, when the shielding effects are not significant. In this section, other uncertainties of the H_2 formation are discussed.

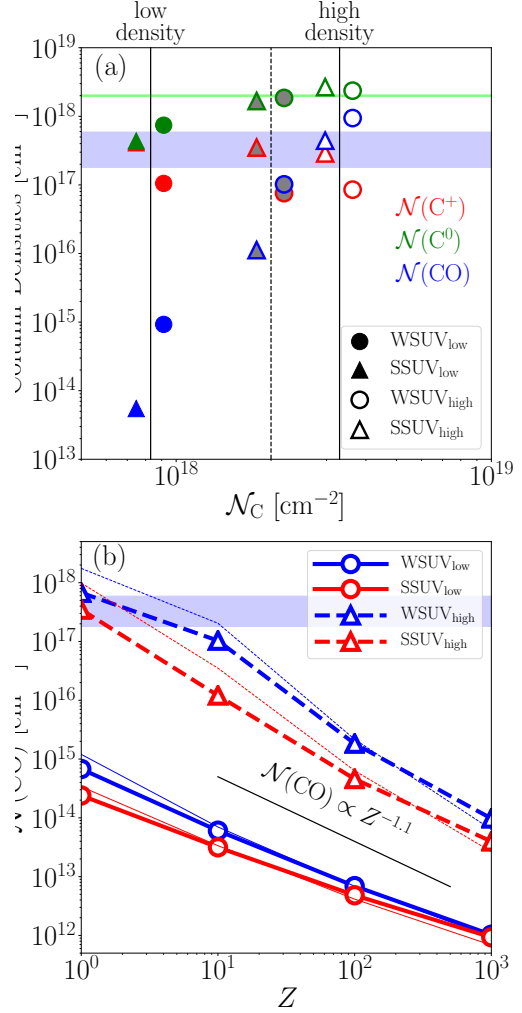


Figure 11. Results of the PDR calculations for 49 Ceti. (a) The mid-plane column densities of (red) C^+ , (green) C^0 , and (blue) CO as a function of \mathcal{N}_{C} for the models with the weak and strong stellar radiation models are shown by the circles and triangles, respectively. The results with $T_{\text{chem}} = 300 \text{ K}$ are shown. The results with the low and high density models are displayed by the filled and open markers. For reference, the results with the intermediate density $n_{\text{C},\text{mid}0} = 1.2 \times 10^3 \text{ cm}^{-3}$ ($\mathcal{N}_{\text{C}} = 2 \times 10^{18} \text{ cm}^{-2}$) are shown by the markers filled by gray. At each \mathcal{N}_{C} , the data points with different stellar models are slightly shifted horizontally for better visibility. The green and blue rectangle regions indicate the observational constraints on the C^0 and CO column densities obtained from Higuchi et al. (2019) and Higuchi et al. (2020), respectively. (b) The mid-plane CO column densities $\mathcal{N}(\text{CO})$ as a function of Z for (blue circles) WSUV_{low} , (red circles) SSUV_{low} , (blue triangles) $\text{WSUV}_{\text{high}}$, and (red triangles) $\text{SSUV}_{\text{high}}$. For each model, the prediction from the analytic formula is shown by the thin line. The blue rectangle region is the same as that in Panel (a). As a reference, $\mathcal{N}(\text{CO}) \propto Z^{-1.1}$ is plotted (Equation (36)).

Another factor not considered in this paper is stochastic effects. Fluctuations of the number of H atoms on the grain surface should be taken into account when few reactive H atoms are on the grain surface (Le Petit et al. 2009). We confirmed that the number density of the H atoms physisorbed on the grain surface is much smaller than the number density of dust grains. This indicates that the master equation should be used instead of the rate equation to accurately estimate the H_2 formation rate of the LH mechanism. Bron et al. (2014) found that the LH mechanism becomes an efficient H_2 formation mechanism in unshielded PDR regions even when the dust temperature is high for the interstellar environment. It is still unknown how the fluctuations of the number of physisorbed H atoms affect H_2 formation in debris disks.

Fluctuations of the dust temperature also affects the H_2 formation for small grains with $a \leq 0.02 \mu\text{m}$ (Cuppen et al. 2006). If only large dust grains exist in debris disks, dust temperature fluctuations are negligible because of their large heat capacities. If small dust grains exist in debris disks, their temperature fluctuations may affect the H_2 formation rate.

4.4. Caveats

Our analytic formula of $n(\text{CO})$ enables us to predict the CO spatial distributions at a given Z and stellar radiation field (Section 4.1). Comparison of our results with observational results gives a constraint on the gas metallicity. In order to confirm whether the steady-state chemistry is a promising mechanism to produce the observed amount of CO, it is crucial to constrain the gas metallicity by other methods.

We should note that the column density of hydrogen is constrained by several observations for the debris disk around β Pictoris. Freudling et al. (1995) obtained an upper limit of the HI column density, $\mathcal{N}(\text{H}^0) < 2 - 5 \times 10^{19} \text{ cm}^{-2}$ from non-detection of the 21 cm line. Lecavelier des Etangs et al. (2001) found that the H_2 column density should be smaller than $\sim 10^{18} \text{ cm}^{-2}$ because H_2 absorption lines are not detected. Using a C^0 column density of $\sim (2.5 \pm 0.7) \times 10^{16} \text{ cm}^{-2}$ (Higuchi et al. 2017), $\mathcal{N}_{\text{C}}/\mathcal{N}_{\text{H}}$ is estimated to be larger than 0.025, which is much larger than $\mathcal{A}_{\text{C,ism}}$. Recently Matrà et al. (2017) constrained the hydrogen number density by the line ratio of CO ($J = 2 - 1$) and CO ($J = 3 - 2$); their result suggests that n_{H} should be smaller than $\sim 10^4 \text{ cm}^{-3}$. If this is the case, the observed CO fractions may not be explained by such a small value of n_{H} even if T_{chem} is sufficiently low. The combination of our results and the observational constraints may rule out the primordial origin ($Z = 1$) of the gas in β Pictoris.

Although we found that there is a parameter set which may explain the amount of CO by considering only steady-state chemical reactions in Sections 4.2.2 and 4.2.3, we need to compare our models with observational results in more detail by performing synthetic observations of our disk models.

For 49 Ceti, Higuchi et al. (2020) showed that the excitation temperatures need to be as low as $\sim 10 \text{ K}$ by conducting non-LTE analysis of the rotational spectral lines of CO considering isotopologues line ratios (also see Kóspál et al. 2013). In our PDR calculations of 49 Ceti, the gas temperatures do not fall below $\sim 20 \text{ K}$. This low excitation temperature may suggest that level populations are not thermalized because of low n_{H} .

We will address direct comparisons between the chemical model and observational results in forthcoming papers.

4.5. Dissipation of Protoplanetary Disks

If the gas in debris disks contains a significant amount of H_2 , the gas of PPDs still remains, at least partially, in debris disks; i.e. the timescale of PPD gas dispersal is longer than the age of debris disks. Many authors investigated the gas dispersal of PPDs through magnetically-driven winds (Suzuki & Inutsuka 2009, 2014) or/and photo-evaporation by UV/X-rays (Hollenbach et al. 1994; Gorti & Hollenbach 2009; Owen et al. 2012; Nakatani et al. 2018). EUV photo-evaporation (Hollenbach et al. 1994) is expected to be inefficient in debris disks around A-type stars because they emit less EUV than either lower and higher mass stars. FUV photo-evaporation would be important at large radii $> 100 \text{ au}$ as long as a large amount of small dust grains exist (Gorti & Hollenbach 2009). During the evolution from a PPD to a debris disk, an amount of dust grains decreases and the grain size increases. Nakatani et al. (2021) recently found that this evolution of dust grains suppress photo-electric heating, making FUV photo-evaporation ineffective. As a result, the lifetime of the gas component is determined by EUV photo-evaporation. Suppose that the EUV flux of an A type star is about $\sim 10^{39} \text{ s}^{-1}$, the photo-evaporation is at least $3 \times 10^{-11} M_{\odot} \text{ yr}^{-1}$ (Gorti et al. 2009). If the initial disk mass at the point small grains have been depleted is $\sim 10^{-3} M_{\odot}$, the lifetime is about 30 Myr, indicating that the lifetime can be longer than 10 Myr. However, the EUV flux in young A-type stars is highly uncertain, and how protoplanetary disks evolve into small-grain-depleted disks are unknown. Further investigations are needed. The future high resolution observation for the C/CO ratio combined with Equation (14) would give the

distribution of n_{H} in depleting PPDs, which may reveal the physics of disk dispersal.

5. SUMMARY

In this paper, we investigated the CO chemistry in optically thin PDRs with larger dust grains than the ISM as a model of debris disks. Because hydrogen is involved in CO formation, the CO abundance should depend on the hydrogen density. This may allow us to constrain the amount of hydrogen if we know how much carbon nuclei becomes CO (Higuchi et al. 2017).

We investigated CO formation only through steady chemical reactions without considering any secondary processes. For simplicity, we consider a stationary plane-parallel semi-infinite uniform slab which is illuminated by the interstellar standard radiation and stellar radiation from its edge. We compute the chemical and thermal equilibria taking into account detailed radiative transfer using the Meudon PDR code (Le Petit et al. 2006; Goicoechea & Le Bourlot 2007; Le Bourlot et al. 2012). Although the plane-parallel geometry is far from the disk geometry, we found that the chemical structure of debris disks can be approximated by the findings from the one-dimensional plane-parallel PDR calculations.

The model parameters are the carbon nucleus density n_{C} , gas metallicity Z , FUV photon number flux χ_{co} that dissociates CO normalized by the Habing flux, the dust-to-gas mass ratio f_{dg} , and T_{chem} , which corresponds to the energy barrier of chemisorption. The model parameters are tabulated in Table 2. We call the models with weaker and strong FUV incident fluxes "weak-FUV" and "strong-FUV", respectively. The dust-to-gas mass ratio is expressed in terms of the carbon nucleus column density at $\tau_{\text{mid}} = 1$ ($\mathcal{N}_{\text{C},\tau_{\text{mid}}=1}$), where τ_{mid} is the mid-plane optical depth (Equation (7)). Observations of debris disks can constrain $\mathcal{N}_{\text{C},\tau_{\text{mid}}=1}$. As a fiducial value of $\mathcal{N}_{\text{C},\tau_{\text{mid}}=1}$, $\mathcal{N}_{\text{C},\tau_{\text{mid}}=1}^{\text{fid}} = 2 \times 10^{19} \text{ cm}^{-2}$ is adopted. The corresponding dust cross section is 80 times smaller than that in the ISM. A fiducial dust-to-gas mass ratio $f_{\text{dg},\text{fid}}$ is defined as f_{dg} at $\mathcal{N}_{\text{C}} = \mathcal{N}_{\text{C},\tau_{\text{mid}}=1}^{\text{fid}}$. The ratio $f_{\text{dg}}/f_{\text{dg},\text{fid}}$ is equal to $(\mathcal{N}_{\text{C},\tau_{\text{mid}}=1}/\mathcal{N}_{\text{C},\tau_{\text{mid}}=1}^{\text{fid}})^{-1}$, and determines the dust surface area (Equation (11)). Considering large uncertainty in H_2 formation on the grain surface, we explore a range of H_2 formation rates on dust grains with a dust temperature of $\sim 100 \text{ K}$ by adopting $T_{\text{chem}} = 300 \text{ K}$ and 10 K . The $T_{\text{chem}} = 10 \text{ K}$ case gives an upper limit of the H_2 formation rate since there is almost no energy barrier in chemisorption.

Our results are summarized as follows:

1. For higher T_{chem} and smaller f_{dg} , we found that CO formation proceeds in the H_2 -poor environments without the influence of H_2 . Our environ-

ments tend to have a very low H_2 abundance because the low grain surface area, high dust temperatures, and low gas temperatures make H_2 formation extremely inefficient if the activation barrier is as high as $T_{\text{chem}} = 300 \text{ K}$. We developed an analytical formula for the CO fractions (Section 3.2). The analytic formula is applicable even in shielded regions by using the local flux attenuated by C^0 and CO, and reproduces the spatial distributions of the CO fractions obtained from the PDR calculations reasonably well (Figure 3).

2. From the high density limit of the analytic formula for $n(\text{CO})/n_{\text{C}}$ (Equation (14)), we obtain the hydrogen nucleus number density required to produce a given $n(\text{CO})/n_{\text{C}}$ as a function of the FUV flux and gas metallicity (Equation (22)). If the amount of carbon nuclei and local FUV flux are fixed, lower metallicity produces a larger amount of CO because there are more H atoms to start the chemistry that produces CO.
3. The H_2 formation rate depends sensitively on T_{chem} since it is proportional to $\exp(-T_{\text{chem}}/T)$. The smaller T_{chem} , the more active the H_2 formation on the grain surface. Increases in f_{dg} also enhances the H_2 formation. The CO formation is accelerated by vibrationally-excited H_2 , whose internal energy is used to overcome an endothermicity of $\text{C}^+ + \text{H}_2 \rightarrow \text{CH}^+ + \text{H}$. The enhancement of the CO fractions owing to the excited H_2 is occurred only when the shielding effects are insignificant. If the shielding effects are important, the CO fractions show different dependence on T_{chem} and f_{dg} . As T_{chem} decreases and/or f_{dg} increases, the CO fractions decrease although the dependence is weak. This is because in such a shielded region, the C^+ fractions is too low for $\text{C}^+ + \text{H}_2 \rightarrow \text{CH}^+ + \text{H}$ to accelerate the CO formation. A decrease in the number of H atoms available for CO formation decreases the CO fractions.
4. A critical dust-to-gas mass ratio $(f_{\text{dg}}/f_{\text{dg},\text{fid}})_{\text{cri}}$ above which the CO formation is accelerated depends sensitively on T_{chem} . For $T_{\text{chem}} = 300 \text{ K}$, roughly speaking, $(f_{\text{dg}}/f_{\text{dg},\text{fid}})_{\text{cri}}$ is about $f_{\text{dg},\text{fid}}$ although it depends on n_{C} and Z (Section 3.3). A decrease of T_{chem} from 300 K to 10 K reduces $(f_{\text{dg}}/f_{\text{dg},\text{fid}})_{\text{cri}}$ significantly; $(f_{\text{dg}}/f_{\text{dg},\text{fid}})_{\text{cri}} \lesssim 0.1$ for weak-FUV and ~ 0.01 for strong-FUV.
5. CO is self-shielded but also shielded by C^0 . Which shielding effect of CO is effective depends on $n(\text{CO})/n_{\text{C}}$ at the low τ limit (Section 3.2.3). For

$n(\text{CO})/n_{\text{C}} > (n(\text{CO})/n_{\text{C}})_{\text{cr}} = 3 \times 10^{-3}$ at $\tau \sim 0$, CO is self-shielded for $N(\text{CO}) > 10^{14} \text{ cm}^{-2}$. When the CO fraction is sufficiently smaller than $(n(\text{CO})/n_{\text{C}})_{\text{cri}}$, the C^0 attenuation increases the CO fraction for $N(\text{C}^0) > 4 \times 10^{16} \text{ cm}^{-2}$ before CO self-shielding becomes important.

6. On the basis of the analytic formula shown in Section 3.2, we developed a method to determine the spatial distributions of the CO number density in a given disk structure by taking into account shielding effects in the radiation field consistently in Section 4.1.

The chemical structure of debris disks have not been studied by taking into account detailed chemical processes consistent with radiation transfer. Particularly, it may be important to consider level populations of H_2 accurately because for lower T_{chem} and/or higher f_{dg} excited H_2 can promote endothermic formation reactions of CH^+ to accelerate the CO formation.

In this paper, an interstellar C/O ratio of 0.4 is used (Table 1). Recently Kama et al. (2016) and Bergin et al. (2016) however found evidence that C/O ratios could exceed unity in PPDs, indicating that C/O ratios change from the interstellar value during the evolution of PPDs. If a part of the gas in a debris disk comes from a remnant PPD, the C/O ratio could exceed unity also in a debris disk. From our analytic formula for the CO fraction (Equation (14)), it is expected that the CO fraction changes in proportion to \mathcal{A}_{O} .

Our results were compared with the observational results of the debris disks around β Pictoris and 49 Ceti in Sections 4.2.2 and 4.2.3, respectively.

For β Pictoris as an example of gas-depleted debris disks, the steady chemical model is difficult to produce a sufficient amount of CO to fit the observational results if the fiducial parameter $T_{\text{chem}} = 300 \text{ K}$ of the Eley-Rideal mechanism for the formation of H_2 on warm dust grains is adopted. The higher the metallicity, the more inefficient CO formation becomes, due to the lack of H atoms to facilitate its formation. The CO column densities decrease as $\propto Z^{-1}$. If T_{chem} is lower than 100 K, the steady chemical model may explain the observed amount of CO due to the H_2 -accelerated CO formation only if $Z \sim 1$ (Figure 9). If $Z > 1$, the steady chemical model cannot produce a sufficient amount of CO even when the H_2 formation on dust surfaces are efficient.

For 49 Ceti as an example of gas-rich debris disks, the CO fraction is sensitive to the column density of carbon nuclei (Figure 11). Our results show that there

is a solution that may explain both the observed CO and C^0 column densities (Higuchi et al. 2020) in a reasonable range of \mathcal{N}_{C} for $Z = 1$ (Higuchi et al. 2019). Since the dust-to-gas mass ratio is extremely small and shielding effects are significant, the CO fraction is insensitive to T_{chem} . As in the case of β Pictoris, the observed CO column density cannot be reproduced for 49 Ceti if $Z > 10$.

We should note that steady state chemical models can explain β Pictoris and 49 Ceti only under a very restricted set of parameters, including enhanced production of H_2 on grains and $Z = 1$. However, for β Pictoris, complementary published observations mentioned in Section 4.4 indicated much lower H or H_2 densities than are required. The combination of this work and the constraints on the H and H_2 reveals that steady state chemistry cannot explain the observations.

As mentioned in Section 1, if the gas in β Pictoris is secondary-origin and CO is supplied from solid bodies through collisions, a required injection rate of CO is estimated by the observed CO mass divided by the CO photo-dissociation timescale. Our results clearly show that the CO formation rate with $Z \gtrsim 1$ is too small to explain the observed amount of CO. The total solid bodies required to provide CO during the stellar age is about $30 M_{\oplus}$ taking into account an expected fraction of CO in the solid bodies (also see Dent et al. 2014). As pointed out in Section 1, we need to consider detailed outgassing processes from solid bodies in order to investigate if the required amount of CO can be supplied. In addition, the gas should be removed at a timescale comparable to the CO photo-dissociation timescale because C^0 and C^+ are accumulated if the gas is not removed. Viscous disk evolution (Kral et al. 2017), EUV photo-evaporation (Nakatani et al. 2021), and disk winds may be important to remove the gas.

We thank the reviewers for providing us many constructive comments that improve this paper significantly. We thank Gianni Cataldi, Satoshi Yamamoto, Nami Sakai, Munetake Momose, Kenji Furuya, and Masanobu Kunitomo for valuable discussions. This work was supported in part by JSPS KAKENHI Grant Numbers 21H00056 (K.I.), 22H00179, 22H01278, 21K03642, 18H05436, 18H05438 (H.K.), 18K03713, 19H05090 (A.E.H.), 18H05222, 20H05844, 20H05847 (Y.A.). Y.A. also acknowledges support by NAOJ ALMA Scientific Research Grant code 2019-13B.

Software: Meudon PDR code (Le Petit et al. 2006), numpy (van der Walt et al. 2011), Matplotlib (Hunter 2007)

APPENDIX

A. AN ANALYTIC FORMULA FOR THE CO FRACTION IN THE SIMPLIFIED CHEMICAL NETWORK WITHOUT HYDROGEN MOLECULE

In this appendix, we construct an analytical model for CO formation by the simplified CO formation network without H_2 shown in Figure 4. With the rate coefficients listed in Table 6, the four chemical balance equations for CO, CO^+ , OH, and CH^+ are solved, where $n(e^-)$ is equal to $n(C^+)$, $n(H)$ is set to be n_H in the H_2 -free environment, most oxygen is in the atomic form ($n(O) \sim n_O$), and the C^0 and C^+ fractions are obtained from Equation (18) with $n(C^+) = n_C - n(C^0)$, where $n(CO) \ll n(C^0)$, $n(C^+)$ is assumed. To investigate the contribution of each path to the CO fraction, the analytical form of the CO fraction is divided into three parts,

$$n(CO)_{\text{ana}} \equiv n(CO)_{\text{oh}} + n(CO)_{\text{chp}} + n(CO)_{\text{woH}}, \quad (\text{A1})$$

where $n(CO)_{\text{oh}}$, $n(CO)_{\text{chp}}$, and $n(CO)_{\text{woH}}$ are the CO fractions formed through the three pathways.

chemical reaction	rate coefficient
$C^+ + H \rightarrow CH^+ + h\nu$	$k_{\text{cp,h}} = 2.29 \times 10^{-17} (T/300)^{-0.42}$
$CH^+ + H \rightarrow H_2 + C^+$	$k_{\text{chp,h}} = 7.5 \times 10^{-10}$
$CH^+ + O \rightarrow CO^+ + H$	$k_{\text{chp,o}} = 3.5 \times 10^{-10}$
$O + H \rightarrow OH + h\nu$	$k_{\text{o,h}} = 9.9 \times 10^{-19} (T/300)^{-0.38}$
$OH + C^+ \rightarrow H + CO^+$	$k_{\text{oh,cp}} = 7.7 \times 10^{-10} (T/300)^{-0.5}$
$OH + C \rightarrow H + CO$	$k_{\text{oh,c}} = 1.0 \times 10^{-10}$
$CO^+ + e^- \rightarrow C + O$	$k_{\text{cop,e}} = 4.58 \times 10^{-7}$
$CO^+ + H \rightarrow CO + H^+$	$k_{\text{cop,h}} = 7.5 \times 10^{-10}$
$OH + h\nu \rightarrow O + H$	$\alpha_{\text{oh}} = 4.3 \times 10^{-6} \chi_{\text{oh}}$
$CO^+ + h\nu \rightarrow C^+ + O$	$\alpha_{\text{cop}} = 1.35 \times 10^{-8} \chi_{\text{co}}^{1.3}$
$CO + h\nu \rightarrow C + O$	$\alpha_{\text{co}} = 10^{-10} \chi_{\text{co}}$

Table 6. Chemical reaction rates that are important in the CO formation shown in Figure 4. The rate coefficients in the first eight reactions are shown in an unit of $\text{cm}^3 \text{s}^{-1}$. The last three rate coefficients correspond to the unattenuated photo-dissociation rates in s^{-1} .

The contributions of the three CO formation paths to the CO fraction for $Z = 1$ and $Z = 10^3$ are illustrated in Figures 12a and 12b, respectively. The spectral type is fixed to A5V. Which CO formation path is important depends both on the gas metallicity and the gas density. For $Z = 1$, CO forms mainly from CH^+ for low densities (Figure 12a). Path_{OH} becomes the dominant pathway to form CO when n_C exceeds $\sim 10 \text{ cm}^{-3}$.

As Z increases, both $n(CO)_{\text{chp}}$ and $n(CO)_{\text{oh}}$ decrease at a fixed n_C since n_H decreases with Z . By contrast, $n(CO)_{\text{woH}}$ is independent of Z at a fixed n_C because hydrogen is not involved in Path_{woH} . As shown in Figure 12b, for $Z = 10^3$, $n(CO)_{\text{woH}}$ dominates over $n(CO)_{\text{chp}}$ by an order of magnitude, and Path_{woH} becomes the dominant pathway to form CO for lower densities. When $n_C > 10^3 \text{ cm}^{-3}$, the CO formation through Path_{OH} determines the CO fraction.

We focus on the high density limit where Path_{OH} is dominant. The path $O \rightarrow OH \rightarrow CO$ contributes to the CO formation more than $O \rightarrow OH \rightarrow CO^+ \rightarrow CO$. Using the fact that the main destruction processes of OH and CO are photo-dissociation, we obtain the CO fraction as follows: The OH abundance is determined by the balance between the radiative association $O + H \rightarrow OH + h\nu$ (the rate coefficient $k_{\text{o,h}}$) and the OH photo-dissociation (the rate coefficient α_{oh}). Eventually, OH is combined with C to form CO with a rate coefficient of $k_{\text{oh,c}}$. Considering the CO photo-dissociation (the rate coefficient α_{co}), the analytical form of the CO fraction is given by

$$\begin{aligned} \frac{n(CO)_{\text{oh}}}{n_C} &= \frac{k_{\text{o,h}} k_{\text{oh,c}}}{\alpha_{\text{co}} \alpha_{\text{oh}}} n_O n_H \\ &= 7.4 \times 10^{-17} T_{300}^{-0.38} \frac{\mathcal{A}_O}{\mathcal{A}_{O,\text{ism}}} \zeta^2, \end{aligned} \quad (\text{A2})$$

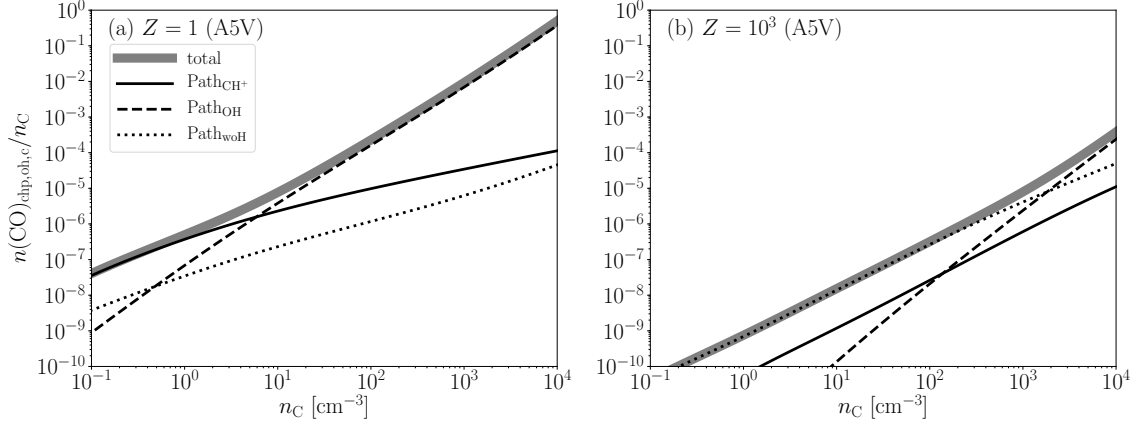


Figure 12. The contributions of the three different paths to the analytic CO fraction as a function of n_C for (a) $Z = 1$ and (b) $Z = 10^3$.

where

$$\zeta = \frac{\sqrt{Z}n_H}{\chi}, \quad \text{where } \chi = \sqrt{\chi_{\text{co}}\chi_{\text{oh}}}, \quad (\text{A3})$$

$T_{300} = T/300$ K, \mathcal{A}_O is the oxygen abundance of the gas phase and $\mathcal{A}_{O,\text{ism}} = 3.2 \times 10^{-4} Z$ (Table 1), and we use the fact that $\alpha_{\text{co}} \propto \chi_{\text{co}}$ and $\alpha_{\text{oh}} \propto \chi_{\text{oh}}$. Equation (A2) shows that the CO fraction depends on $n_H Z^{0.5} \chi^{-1}$, which is quite similar to η . The difference between η and $Z^{0.5} n_H \chi^{-1}$ comes from the temperature dependence shown in Equation (A2).

Equation (A2) shows that $n(\text{CO})_{\text{ana}}$ is expected to be characterized by ζ at least for high densities where $n(\text{CO})_{\text{ana}} \sim n(\text{CO})_{\text{oh}}$. In order to check this, we fit $n(\text{CO})_{\text{ana}}$ with a function of $\eta = n_H Z^a \chi^b$, where a and b are the fitting parameters. As shown in Figure 13, we found that $n(\text{CO})_{\text{ana}}$ is insensitive to both Z and χ for $\eta > 10^5 \text{ cm}^{-3}$ if η with $a = 0.4$ and $b = -1.1$ is taken as the horizontal axis. The difference between ζ and η with $a = 0.4$ and $b = -1.1$ comes from the negative temperature dependence of $n(\text{CO})_{\text{oh}}$ (Equation (A2)). The gas temperatures increase when either Z or χ increases. Even for low densities where Path_{OH} is no longer dominant CO formation path, $n(\text{CO})_{\text{ana}}$ is characterized by $\eta = n_H Z^{0.4} \chi^{-1.1}$ reasonably well. A fitting function of the CO fraction is given by

$$\frac{n(\text{CO})_{\text{ana}}}{n_C} = \frac{\mathcal{A}_O}{\mathcal{A}_{O,\text{ism}}} (10^{-14} \eta^{1.8} + 6.0 \times 10^{-11} \eta). \quad (\text{A4})$$

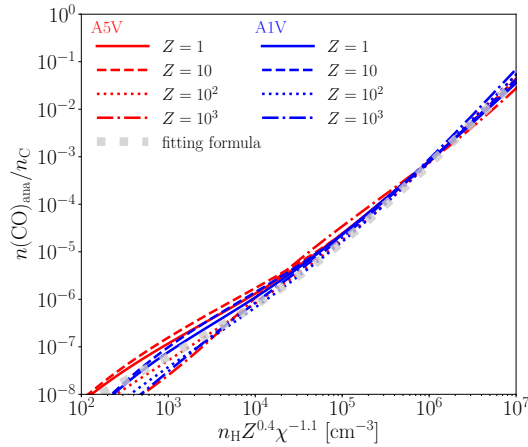


Figure 13. The CO fraction estimated by Equation (A1) for various metallicities and spectral types. The horizontal axis is $\eta = n_H Z^{0.4} \chi^{-1.1} = \zeta(Z\chi)^{-0.1}$. The gray dotted line corresponds to the fitting function shown by Equation (A4).

REFERENCES

- Ádámkóvics, M., Glassgold, A. E., & Meijerink, R. 2011, *ApJ*, 736, 143
- Agúndez, M., Goicoechea, J. R., Cernicharo, J., Faure, A., & Roueff, E. 2010, *ApJ*, 713, 662
- Ahrens, T. J., & O’Keefe, J. D. 1972, *Moon*, 4, 214
- Bakes, E. L. O., & Tielens, A. G. G. M. 1994, *ApJ*, 427, 822
- Bergin, E. A., Du, F., Cleaves, L. I., et al. 2016, *ApJ*, 831, 101
- Bertoldi, F., & Draine, B. T. 1996, *ApJ*, 458, 222
- Bron, E., Le Boulrot, J., & Le Petit, F. 2014, *A&A*, 569, A100
- Burns, J. A., Lamy, P. L., & Soter, S. 1979, *Icarus*, 40, 1
- Cataldi, G., Brandeker, A., Olofsson, G., et al. 2014, *A&A*, 563, A66
- Cataldi, G., Brandeker, A., Wu, Y., et al. 2018, *ApJ*, 861, 72
- Chen, C. H., Sargent, B. A., Bohac, C., et al. 2006, *ApJS*, 166, 351
- Compiègne, M., Verstraete, L., Jones, A., et al. 2011, *A&A*, 525, A103
- Cuppen, H. M., Morata, O., & Herbst, E. 2006, *MNRAS*, 367, 1757
- Dent, W. R. F., Wyatt, M. C., Roberge, A., et al. 2014, *Science*, 343, 1490
- Dohnanyi, J. S. 1969, *J. Geophys. Res.*, 74, 2531
- Draine, B. T. 1978, *ApJS*, 36, 595
- Draine, B. T., & Bertoldi, F. 1996, *ApJ*, 468, 269
- Draine, B. T., & Li, A. 2001, *ApJ*, 551, 807
- Federman, S. R., Glassgold, A. E., & Kwan, J. 1979, *ApJ*, 227, 466
- Fernández, R., Brandeker, A., & Wu, Y. 2006, *ApJ*, 643, 509
- Freudling, W., Lagrange, A.-M., Vidal-Madjar, A., Ferlet, R., & Forveille, T. 1995, *A&A*, 301, 231
- Genda, H., Kobayashi, H., & Kokubo, E. 2015, *ApJ*, 810, 136
- Goicoechea, J. R., & Le Boulrot, J. 2007, *A&A*, 467, 1
- Goicoechea, J. R., & Roncero, O. 2022, *A&A*, 664, A190
- Goicoechea, J. R., Pety, J., Cuadrado, S., et al. 2016, *Nature*, 537, 207
- Gorti, U., Dullemond, C. P., & Hollenbach, D. 2009, *ApJ*, 705, 1237
- Gorti, U., & Hollenbach, D. 2004, *ApJ*, 613, 424
- . 2009, *ApJ*, 690, 1539
- Grigorieva, A., Thébault, P., Artymowicz, P., & Brandeker, A. 2007, *A&A*, 475, 755
- Habart, E., Abergel, A., Boulanger, F., et al. 2011, *A&A*, 527, A122
- Habing, H. J. 1968, *Bull. Astron. Inst. Netherlands*, 19, 421
- Haisch, Jr., K. E., Lada, E. A., & Lada, C. J. 2001, *ApJL*, 553, L153
- Heap, S. R., Lindler, D. J., Lanz, T. M., et al. 2000, *ApJ*, 539, 435
- Heays, A. N., Bosman, A. D., & van Dishoeck, E. F. 2017, *A&A*, 602, A105
- Herráez-Aguilar, D., Jambrina, P. G., Menéndez, M., et al. 2014, *Physical Chemistry Chemical Physics (Incorporating Faraday Transactions)*, 16, 24800
- Hierl, P. M., Morris, R. A., & Viggiano, A. A. 1997, *JChPh*, 106, 10145
- Higuchi, A. E., Kóspál, Á., Moór, A., Nomura, H., & Yamamoto, S. 2020, *ApJ*, 905, 122
- Higuchi, A. E., Sato, A., Tsukagoshi, T., et al. 2017, *ApJL*, 839, L14
- Higuchi, A. E., Saigo, K., Kobayashi, H., et al. 2019, submitted in *ApJ*
- Hollenbach, D., Johnstone, D., Lizano, S., & Shu, F. 1994, *ApJ*, 428, 654
- Howarth, I. D. 2011, *MNRAS*, 413, 1515
- Hughes, A. M., Duchêne, G., & Matthews, B. C. 2018, *ARA&A*, 56, 541
- Hughes, A. M., Wilner, D. J., Kamp, I., & Hogerheijde, M. R. 2008, *ApJ*, 681, 626
- Hughes, A. M., Lieman-Sifry, J., Flaherty, K. M., et al. 2017, *ApJ*, 839, 86
- Hunter, J. D. 2007, *Computing in Science and Engineering*, 9, 90
- Ivanovskaya, V. V., Zobelli, A., Teillet-Billy, D., et al. 2010, *PhRvB*, 82, 245407
- Iwasaki, K., Tanaka, H., Nakazawa, K., & Hiroyuki, E. 2001, *PASJ*, 53, 321
- Joblin, C., Bron, E., Pinto, C., et al. 2018, *A&A*, 615, A129
- Jura, M. 1974, *ApJ*, 191, 375
- Jura, M., Malkan, M., White, R., et al. 1998, *ApJ*, 505, 897
- Jura, M., Zuckerman, B., Becklin, E. E., & Smith, R. C. 1993, *ApJL*, 418, L37
- Kama, M., Bruderer, S., van Dishoeck, E. F., et al. 2016, *A&A*, 592, A83
- Kamp, I., & Bertoldi, F. 2000, *A&A*, 353, 276
- Kamp, I., van Zadelhoff, G.-J., van Dishoeck, E. F., & Stark, R. 2003, *A&A*, 397, 1129
- Kobayashi, H., & Löhne, T. 2014, *MNRAS*, 442, 3266
- Kobayashi, H., & Tanaka, H. 2010, *Icarus*, 206, 735
- Kobayashi, H., Watanabe, S., Kimura, H., & Yamamoto, T. 2008, *Icarus*, 195, 871
- . 2009, *Icarus*, 201, 395
- Kóspál, Á., Moór, A., Juhász, A., et al. 2013, *ApJ*, 776, 77

- Kral, Q., Marino, S., Wyatt, M. C., Kama, M., & Matrà, L. 2019, *MNRAS*, 489, 3670
- Kral, Q., Matrà, L., Wyatt, M. C., & Kennedy, G. M. 2017, *MNRAS*, 469, 521
- Kral, Q., Wyatt, M., Carswell, R. F., et al. 2016, *MNRAS*, 461, 845
- Kraus, R. G., Senft, L. E., & Stewart, S. T. 2011, *Icarus*, 214, 724
- Kurosawa, K., Sugita, S., Kadono, T., et al. 2010, *Geophys. Res. Lett.*, 37, L23203
- Kurucz, R. L. 1992, *RMxAA*, 23, 181
- Laor, A., & Draine, B. T. 1993, *ApJ*, 402, 441
- Lavendy, H., Robbe, J. M., & Flament, J. P. 1993, *Chemical Physics Letters*, 205, 456
- Le Bourlot, J., Le Petit, F., Pinto, C., Roueff, E., & Roy, F. 2012, *A&A*, 541, A76
- Le Petit, F., Barzel, B., Biham, O., Roueff, E., & Le Bourlot, J. 2009, *A&A*, 505, 1153
- Le Petit, F., Nehmé, C., Le Bourlot, J., & Roueff, E. 2006, *ApJS*, 164, 506
- Lecavelier des Etangs, A., Vidal-Madjar, A., Roberge, A., et al. 2001, *Nature*, 412, 706
- Lodders, K. 2008, *ApJ*, 674, 607
- Mathis, J. S., Mezger, P. G., & Panagia, N. 1983, *A&A*, 128, 212
- Mathis, J. S., Rumpl, W., & Nordsieck, K. H. 1977, *ApJ*, 217, 425
- Matrà, L., Panić, O., Wyatt, M. C., & Dent, W. R. F. 2015, *MNRAS*, 447, 3936
- Matrà, L., Wilner, D. J., Öberg, K. I., et al. 2018, *ApJ*, 853, 147
- Matrà, L., Dent, W. R. F., Wyatt, M. C., et al. 2017, *MNRAS*, 464, 1415
- Mennella, V. 2006, *ApJL*, 647, L49
- Meyer, D. M., Cardelli, J. A., & Sofia, U. J. 1997, *ApJL*, 490, L103
- Meyer, D. M., Jura, M., & Cardelli, J. A. 1998, *ApJ*, 493, 222
- Mizuno, H., Nakazawa, K., & Hayashi, C. 1978, *Progress of Theoretical Physics*, 60, 699
- Montesinos, B., Eiroa, C., Mora, A., & Merín, B. 2009, *A&A*, 495, 901
- Moór, A., Kral, Q., Ábrahám, P., et al. 2019, *ApJ*, 884, 108
- Morton, D. C. 1975, *ApJ*, 197, 85
- Nakatani, R., Hosokawa, T., Yoshida, N., Nomura, H., & Kuiper, R. 2018, *ApJ*, 865, 75
- Nakatani, R., Kobayashi, H., Kuiper, R., Nomura, H., & Aikawa, Y. 2021, *ApJ*, 915, 90
- Navarro-Ruiz, J., Martínez-González, J. Á., Sodupe, M., Ugliengo, P., & Rimola, A. 2015, *MNRAS*, 453, 914
- Navarro-Ruiz, J., Sodupe, M., Ugliengo, P., & Rimola, A. 2014, *Physical Chemistry Chemical Physics (Incorporating Faraday Transactions)*, 16, 17447
- Okeefe, J. D., & Ahrens, T. J. 1982, *J. Geophys. Res.*, 87, 6668
- Ootsubo, T., Kawakita, H., Hamada, S., et al. 2012, *ApJ*, 752, 15
- Owen, J. E., Clarke, C. J., & Ercolano, B. 2012, *MNRAS*, 422, 1880
- Roberge, A., Feldman, P. D., Lagrange, A. M., et al. 2000, *ApJ*, 538, 904
- Roberge, A., Feldman, P. D., Weinberger, A. J., Deleuil, M., & Bouret, J.-C. 2006, *Nature*, 441, 724
- Roberge, A., Kamp, I., Montesinos, B., et al. 2013, *ApJ*, 771, 69
- Savage, B. D., & Sembach, K. R. 1996, *ARA&A*, 34, 279
- Sha, X., Jackson, B., & Lemoine, D. 2002, *JChPh*, 116, 7158
- Sternberg, A., Gurman, A., & Bialy, S. 2021, *ApJ*, 920, 83
- Sultanov, R. A., & Balakrishnan, N. 2005, *ApJ*, 629, 305
- Suzuki, T. K., & Inutsuka, S.-i. 2009, *ApJL*, 691, L49
- . 2014, *ApJ*, 784, 121
- Tanaka, H., Inaba, S., & Nakazawa, K. 1996, *Icarus*, 123, 450
- Tanigawa, T., & Ikoma, M. 2007, *ApJ*, 667, 557
- Tieftrunk, A., Pineau des Forets, G., Schilke, P., & Walmsley, C. M. 1994, *A&A*, 289, 579
- van der Walt, S., Colbert, S. C., & Varoquaux, G. 2011, *Computing in Science and Engineering*, 13, 22
- van Dishoeck, E. F., & Black, J. H. 1988, *ApJ*, 334, 771
- van Dishoeck, E. F., & Dalgarno, A. 1983, *JChPh*, 79, 873
- . 1984, *ApJ*, 277, 576
- van Dishoeck, E. F., Jonkheid, B., & van Hemert, M. C. 2006, *Faraday Discussions*, 133, 231
- Veselinova, A., Agúndez, M., Goicoechea, J. R., et al. 2021, *A&A*, 648, A76
- Visser, R., van Dishoeck, E. F., & Black, J. H. 2009, *A&A*, 503, 323
- Weaver, H. A., Feldman, P. D., A’Hearn, M. F., Dello Russo, N., & Stern, S. A. 2011, *ApJL*, 734, L5
- Wishart, A. W. 1979, *MNRAS*, 187, 59P
- Zanchet, A., Agúndez, M., Herrero, V. J., Aguado, A., & Roncero, O. 2013a, *AJ*, 146, 125
- Zanchet, A., Godard, B., Bulut, N., et al. 2013b, *ApJ*, 766, 80
- Zecho, T., Guttler, A., Sha, X., Jackson, B., & Kuppers, J. 2002, *JChPh*, 117, 8486